applied sciences

MDPI

Article

EsTRACE—Es-Layer TRAnsient Cloud Explorer: PlanarSat Mission Concept and Early-Phase Design (Bid, CoDR, PDR) for Sporadic-E Sensing

Mehmet Şevket Uludağ [1,2,*] and Alim Rüstem Aslan [2]

[1] Faculty of Aerospace Engineering, Delft University of Technology, Kluyverweg 1, 2629 HS Delft, The Netherlands
[2] Faculty of Aeronautics and Astronautics, Istanbul Technical University, Ayazağa Campus, 34469 Maslak, Istanbul, Turkey; aslanr@itu.edu.tr
* Correspondence: m.s.uludag@tudelft.nl

Abstract

Sporadic-E (Es) layers can strongly perturb HF/VHF propagation and create intermittent interference, motivating higher-revisit monitoring at the frequencies most affected. EsTRACE (Es-layer TRAnsient Cloud Explorer) is a PlanarSat mission concept that transmits sequential beacons in the 28/50 MHz amateur bands using FT4 (weak-signal digital) and CW (continuous wave) waveforms and leverages distributed amateur receiver networks for near-real-time SNR mapping. This paper documents the early-phase spacecraft design from the Bid/proposal phase (Bid), through the Conceptual Design Review (CoDR), to the Preliminary Design Review (PDR), using a power-first sizing loop that couples link-budget closure to duty cycle and solar-array area under a free-tumbling, batteryless constraint. The analysis supports conceptual feasibility of the architecture under stated antenna and ground-segment assumptions; on-orbit demonstration and measured RF/antenna characterization are identified as required future validation steps.

Keywords: PlanarSat; Attosat; Femtosat; small satellite; ChipSat; systems engineering; sporadic E; space weather

1. Introduction

Sporadic-E (Es) is a transient phenomenon in which thin, high–electron-density layers form within the Earth's E-region ionosphere, typically at altitudes of ∼90–130 km, with vertical thicknesses of ∼1–5 km and horizontal extents up to hundreds or even >1000 km [1–3]. Unlike the comparatively stable background E layer that follows solar and diurnal cycles, Es is irregular in occurrence, duration (minutes to hours), and location [2–4]. Formation is widely attributed to wind-shear convergence of long-lived metallic ions sourced from meteoric ablation; at high and low latitudes, auroral electrodynamics and thunderstorm-associated electric fields can also contribute [1–3].

Operationally, Es strongly perturbs radio-wave propagation. It can reflect frequencies up to ∼150 MHz, enabling long-range skip communication for very-high-frequency (VHF, 30–300 MHz) services that would otherwise be line-of-sight limited; high-frequency (HF, 3–30 MHz) links are also strongly affected by absorption and mode conversion during disturbed conditions [1,2,4]. While occasionally beneficial, this same mechanism introduces unpredictable interference and can degrade radar and navigation performance, which is a concern for safety-critical domains such as aviation, emergency services, and positioning [4–6].

Academic Editor: Ephraim Suhir

Received: 20 November 2025
Revised: 21 December 2025
Accepted: 29 December 2025
Published: 30 December 2025

Consequently, the timely detection and mapping of Es is valuable both for frequency management and for maintaining service reliability [5,6].

Existing techniques for sensing Es layers each have significant limitations. Sounding rockets and ground-based ionospheric sounders (ionosondes) can directly probe Es layers with fine vertical resolution, but these measurements are confined to a narrow overhead column at specific locations and times, yielding excellent height profiles but very sparse spatial coverage [7,8]. Global statistics on Es occurrence can be obtained via GNSS radio occultation (GNSS-RO) using L-band signals (roughly ∼1.2–1.6 GHz depending on system and frequency), yet Es signatures at these frequencies are inferred indirectly (e.g., excess phase or scintillation proxies) and require modeling assumptions to map the observables to Es intensity, introducing notable uncertainties [9–11]. In addition, the dispersive ionospheric group delay scales as $1/f^2$; therefore, for a comparable electron-content perturbation, a 28–50 MHz beacon experiences $\sim 10^3$–$10^{3.5}$ times larger phase/delay sensitivity than L-band, making HF/VHF-low beacons inherently more responsive to Es-induced propagation perturbations [12]. In this work, we therefore compare approaches primarily by the operational observable (direct HF/VHF propagation perturbation vs. indirect L-band proxy) and by frequency-scaled sensitivity, rather than by attempting an electron-density retrieval accuracy comparison across fundamentally different measurement modalities.

Ground-based monitoring approaches (for example HF/VHF radars and distributed receiver networks) similarly demand substantial infrastructure and are constrained to their installation sites, leaving large portions of the globe such as oceans or remote regions unobserved [1]. Consequently, there is still no low-cost, space-based, high-revisit system dedicated to monitoring sporadic E in the HF/VHF radio bands, precisely the frequencies where Es can most strongly disrupt communications and radar operations [13].

To address these limitations, Vanhamel et al. propose a low-cost, space-based concept that flies dual-frequency beacons (FT4 and CW at 28/50 MHz) and exploits the global amateur-radio receiving ecosystem (for example OpenWebRX (web-accessible software-defined-radio receiver software), WSPR, and RBN) for distributed, near-real-time SNR-based detection [1]. This leverages existing ground infrastructure to improve coverage and scalability, whereas conventional space methods such as GNSS-RO operate at much higher frequencies and with different dominant error sources [1]. At $h \approx 550$ km, the geometric footprint radius is ∼2060 km for $\varepsilon \geq 5^\circ$ (diameter ∼4120 km); actual sampling depends on receiver locations.

Table 1 compares these approaches across coverage/revisit, primary observable/Es sensitivity, and infrastructure burden; this qualitative summary is not intended as a ranking but as a guide to complementary strengths and limitations.

This paper (i) adapts the Es beacon concept to a PlanarSat spacecraft architecture and explicitly links link-budget closure to power-first spacecraft sizing; (ii) provides a phase-by-phase design trace (Bid/CoDR/PDR) that quantifies the coupling between transmit power, duty cycle, and solar-array area under batteryless constraints; and (iii) frames operations in terms of an explicit operational power envelope under free-tumbling attitude, enabling transparent feasibility bounds and future refinement with measured RF/antenna characteristics.

Table 1. Qualitative comparison of Es sensing approaches in key performance dimensions (coverage/revisit, operational data footprint, and sensitivity/observable). Where published quantitative values are mission dependent or not present in this manuscript, we report qualitative capability and explicitly note the limitation.

Approach	Coverage/Revisit	Primary Observable and Es Sensitivity	Data Rate/Infrastructure
EsTRACE (this work): LEO HF/VHF-low beacon at 28/50 MHz + distributed receivers	Potentially near-global sampling where receivers exist; rapid revisit along orbit tracks; scalable via multiple PlanarSats	Directly measures Es impact on HF/VHF propagation at operationally relevant frequencies; detectability thresholds defined by FT4/CW weak-signal limits [1]	Very low on-air bit rates (FT4: 34.5 bit/s; CW: 16.7 bit/s); leverages existing receiver networks (OpenWebRX/WSPR/RBN) [1,14]
GNSS-RO at L-band (∼1.2–1.6 GHz)	Near-global sampling with multi-satellite constellations; profiles along occultation rays	Es inferred indirectly (e.g., excess phase/scintillation proxies) and model-dependent; dispersive response scales as $1/f^2$ and is much weaker than at 28–50 MHz for comparable perturbations [9–12]	Requires GNSS-RO receiver payload and occultation geometry; processed profiles downlinked; does not rely on amateur infrastructure
Ground ionosondes/HF–VHF radars	Regional coverage where installed; sparse over oceans/remote regions	Direct sounding/backscatter; good altitude resolution over station; limited to fixed sites [7,8]	Requires dedicated ground infrastructure and operations
Sounding rockets	Campaign/event-based; point measurements	In situ, very high vertical resolution; limited duration and geography	High cost per event; not continuous monitoring

Satellite Form

Satellite miniaturization has reshaped the small-spacecraft landscape across the last two decades, enabling rapid iteration cycles, lower hardware cost, and distributed sensing concepts that were difficult to justify with larger buses [15]. Within this trend, sub-100 g spacecraft have emerged in two mass-based classes, femtosatellites and attosatellites, and their designs increasingly converge toward flat, single-plane boards that use one or both faces for functionality. To avoid ambiguity and emphasize geometry rather than mass alone, recent work has proposed the umbrella term PlanarSat for this family of highly miniaturized, planar spacecraft [16]. At these scales, shared design drivers such as surface-limited power generation, component placement on a single PCB or flexible substrate, and access-to-space via a host mothership tend to dominate over mass alone [16].

Early demonstrations established both feasibility and limits. Pocket-PUCP was deployed from PUCP-SAT-1 in 2013 as a secondary temperature probe that relayed data through its CubeSat carrier [17]. China's Stardust femtosatellites (2015) rode attached to larger spacecraft to test distributed magnetometry and environmental survivability [18]. Cornell's Sprite devices ultimately achieved the first free-flying attosatellites in 2019 via KickSat-2, showing that gram-scale boards can self-transmit from orbit if the power and link budgets are tuned to extreme constraints [19,20]. More recently, SUCHAI-3 deployed femtosatellites to study localization from inter-satellite links, underscoring a pattern in which the small boards act as the payload and the CubeSat provides logistics, telemetry downlink, and regulatory compliance [21]. Active attitude control can mitigate orientation variability and improve link predictability even for microspacecraft, but it typically competes directly with the stringent power, volume, and complexity constraints of batteryless PlanarSats; a recent survey of embedded microspacecraft attitude-control designs provides context for this trade [22]. Together these missions motivate a design-based class that captures

planar form factor, deployment dependencies, and surface-limited power as first-order concerns [16].

Within this design space, EsTRACE (Es-layer TRAnsient Cloud Explorer) is a PlanarSat mission that is designed to enable multi-node measurements of sporadic-E phenomena. The PlanarSat architecture is a quasi-two-dimensional, single-plane layout in which one or both faces of a flat substrate are populated with satellite subsystems [16]. The concept has its roots in the evolution of ChipSat (gram-scale, chip-integrated satellites) and PCB-Sat (printed-circuit-board satellites) prototypes, but it is defined here as a more broadly applicable architecture with a formal design framework extending beyond any specific mass category [23,24]. At these extreme miniaturization scales, traditional classifications based solely on mass (for example femto- or attosatellite classes) become inadequate, motivating a taxonomy centered on form factor rather than mass [16]. This planar form factor enables low-cost distributed sensor constellations and planetary exploration swarms that are impractical for larger satellites, while also imposing unique structural and integration constraints since all functionality must be confined to a thin, surface-constrained volume with limited power and aperture for payloads [16].

At the ultra-small end of spacecraft design, feasibility is governed by power and surface area rather than mass. The PlanarSat architecture, in which the payload, transceiver, OBC, PCDU, and solar cells must co-exist on the same limited area, captures this constraint [16]. Prior work introduced a power-first sizing methodology with phase-appropriate contingencies and an operational power envelope (OPE) that makes orientation and duty-cycle limits explicit [25,26]. In this paper, we adapt that method to the Es-beacon use case: the link budget sets transmit power and duty cycle; these, in turn, dimension the array area under a free-tumbling attitude assumption. We focus on a single-payload minimal bus and reserve constellation scaling for an outlook.

This paper presents the development across the main design phases of the project. We start with a brief description of the payload (RABSII) and then explain the calculations and design choices made during the Bidding phase (Bid), conceptual design review (CoDR), and Preliminary design review (PDR) phases.

2. Mission Concept and Payload/Bus Scope

We adopt the single-frequency, sequential beacon approach in the 28 or 50 MHz amateur bands [1]. Specifically, the payload alternates FT4 (a weak-signal, time-synchronized digital mode) and continuous-wave (CW) transmissions at 28/50 MHz [14,27]. FT4 offers robust weak-signal operation using time-synchronized CPFSK (Continuous-Phase Frequency-Shift Keying) with forward error correction, while CW provides a complementary higher-SNR (signal-to-noise ratio) reference [14,27]. Reported network performance indicates FT4 detectability near -17.5 dB SNR and CW near -1 dB SNR; these levels are used as design thresholds [1]. Reception and SNR estimation rely on existing amateur ecosystems such as OpenWebRX (web-accessible software-defined-radio receivers), WSPR (Weak Signal Propagation Reporter), and RBN (Reverse Beacon Network) [1,14].

The initial mission is single satellite and single sensor to minimize complexity and cost while preserving payload-centric flexibility. Prior guidance highlights that single-sensor platforms pair well with small buses and rideshare delivery and reduce inter-sensor interference [28] (p. 41). At the same time, small satellites may help enable low-cost missions, but small does not guarantee low cost [28] (p. 2).

The payload flies on a minimal, single-sensor bus in a PlanarSat form factor, where payload, transceiver, OBC, PCDU, and solar cells share the same limited area and power budget [16]. No propulsion is included. The baseline attitude is free-floating with realistic disturbances (solar radiation pressure, gravity-gradient, and aerodynamic torques).

For power sizing, we use a conservative cosine-incidence model about the sun vector (see Section 5.2), consistent with power-first practice [25,26]. The reference orbit is a circular sun-synchronous rideshare at 520–580 km [29].

The design proceeds with a power-first loop [25,26]: (i) build link budgets at 28/50 MHz using the FT4/CW detection thresholds and representative ground-station SNR distributions [1]; (ii) derive required transmitter power and duty cycle from detectability constraints; (iii) translate these to the array area; (iv) allocate bus peripherals and compute current best estimate (CBE) power with contingencies [25]; and (v) verify the operational power envelope across seasonal illumination and attitude variations.

Operations assume rideshare insertion near 525 km $\pm$ 25 km. Instantaneous beacon coverage sets how many ground stations are illuminated per pass and thus the probability of detection and geolocation of Es occurrences [1]. The above steps provide early, quantitative trades between batteryless and with-battery operation, array area, and achievable duty cycle, suitable for pre-PDR milestones through CoDR, with payload constraints taken at Bid and refined through CoDR [25].

If EsTRACE is scaled to a constellation, simultaneous co-channel FT4/CW transmissions from multiple satellites could create avoidable mutual interference at common receivers. A practical mitigation is GNSS-synchronized orthogonalization: (i) assign each satellite a deterministic time slot (TDMA: Time-Division Multiple Access) aligned to the FT4 frame timing [1,30,31], and/or (ii) apply small center-frequency offsets within the allocated amateur sub-band so that concurrent transmissions remain separable [31,32]. Unique identifiers embedded in each frame (callsign/locator) then allow network-side association of detections to a specific spacecraft [1,30]. This concept-of-operations item is retained as a scalability requirement for future multi-node deployments.

A full constellation capacity and interference assessment (including dependence on the number of simultaneous transmitters N and regulatory coordination constraints) is retained as future work.

The following Level-1, shown in Table 2, requirements drive the design and analyses that follow. They are stated to be specific, measurable, and verifiable, and they trace to the Es detection concept and PlanarSat constraints [1,14,16,25–27,29].

Table 2. Level-1 system requirements and verification approach.

ID	Requirement
SR-1	The payload shall transmit sequential FT4 and CW beacons in the 28 MHz or 50 MHz amateur bands.
SR-2	The system shall achieve detectability at FT4 network SNR near -17.5 dB and CW near -1 dB using distributed amateur networks (for example OpenWebRX/WSPR/RBN) at the reference orbit [1,14].
SR-3	FT4 transmissions shall align to GNSS time boundaries (7.5 s frames with 5.04 s on-time) per protocol [27].
SR-4	The spacecraft shall operate without propulsion and in a free-floating attitude.
SR-5	Average and peak electrical power shall not exceed what is available from the solar array.
SR-6	The reference orbit shall be circular SSO at 550 $\pm$ 25 km.
SR-7	Telemetry shall provide beacon health and timing sufficient for SNR mapping and ground correlation.

3. Concept Feasibility—Bid

This mission aims to create a low-cost infrastructure for Sporadic-E detection at 28 MHz and 50 MHz and a technology demonstration for PlanarSats. Es events are detected via differential Signal-to-noise Ratio (SNR) (FT4 vs. CW) at 28/50 MHz. Oc-

currence/coverage statistics are produced along orbit tracks with community receivers. Ultra-low-power beacon feasibility is demonstrated on a PlanarSat. A payload is being developed by [1]. Early stage payload is approximately $70 \times 100 \times 10$ mm with a power consumption of 300 mW at peak and 100 mW idle [1]. Payload also requires position data to be included in the beacon in order to locate the Sporadic-E cloud.

The basic signal chain is MCU/OBC logic $\rightarrow$ Es payload $\rightarrow$ antenna(s), with an onboard Global Navigation Satellite System (GNSS) receiver providing timing and position tags for the beacon frames. The Electrical Power System (EPS) is a direct-solar, regulated bus, and to minimize complexity and cost the Bid phase assumes batteryless, daylight-only operation. The spacecraft carries no active attitude-control hardware: at $\sim$550 km altitude the high area-to-mass ratio of the planar body leads to appreciable aerodynamic and gravity-gradient torques that passively damp rotation and bias the attitude toward low-rate, broadside-to-velocity orientations over time [16], so operations are designed for such passively stabilized, slowly varying attitudes rather than precise pointing. Within this framework, the beacon is duty-cycled (e.g., 15 s FT4 / 15 s CW) with daylight-preferred transmissions, and the PlanarSat operates in two main modes: a payload (science) mode, in which the Es beacon is active, and a Telemetry, Tracking, and Command (TT&C) mode for housekeeping and command; the resulting quasi-2D frame-like layout is shown in Figure 1.

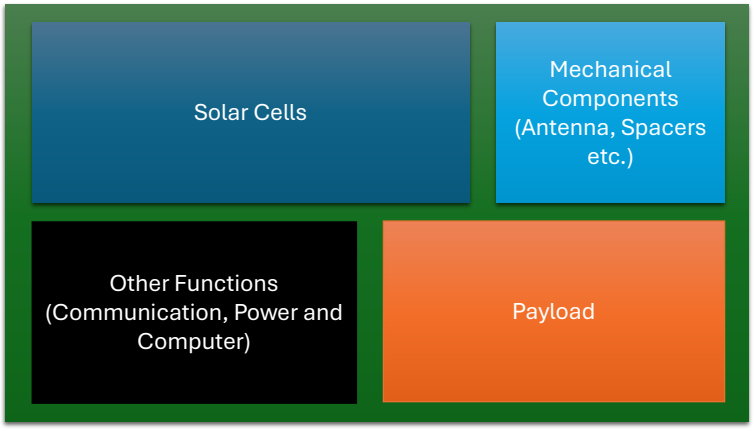

Figure 1. Basic system architecture.

3.1. Initial Link Budget

We use a G/T-based downlink model. The ground station is represented by its figure of merit G/T (dB/K); receive-side gain, losses, and system temperature are therefore not re-applied elsewhere [33]. The satellite transmit side enters only through the EIRP. Constants in this phase are $(G/T) = -25$ dB/K, $G_{T_x} = -25$ dBi, $L_{T_x} = 0.5$ dB, and altitude $h = 550$ km. Importantly, G_{T_x} is interpreted as an effective realized gain in the direction of the ground station (i.e., including mismatch, pattern non-idealities, and attitude variability), not as an isotropic-radiator assumption. The sensitivity of $\mathcal{M}$ to degraded realized G_{T_x}, degraded receiving-site (G/T), and additional unmodeled losses is quantified in Section 4.1.

The slant range versus elevation ε (deg) is

$$d_{\mathrm{km}}(\varepsilon) = \sqrt{(R_E + h)^2 - \left(R_E \cos\varepsilon\right)^2} - R_E \sin\varepsilon. \tag{1}$$

Free-space loss (FSPL) and the path term used in the calculations are

$$L_{\mathrm{FS}}(f, \varepsilon) = 32.45 + 20\log_{10}(f_{\mathrm{MHz}}) + 20\log_{10}(d_{\mathrm{km}}(\varepsilon)), \tag{2}$$

$$L_{\text{path}}(f,\varepsilon) = L_{\text{FS}}(f,\varepsilon) + L_{\text{pol}} + L_{\text{wet}} + L_{\text{dry}} + L_{\text{ion}} + L_{\text{pnt}}, \tag{3}$$

where the FSPL follows [34] and the small, elevation-independent allowances are $L_{\text{pol}} = 3.0$ dB, $L_{\text{wet}} \approx 1.8 \times 10^{-5}$ dB, $L_{\text{dry}} = 0.01$ dB, $L_{\text{ion}} = 0.2$ dB, $L_{\text{pnt}} = 0.1$ dB. (At 28–50 MHz, tropospheric gaseous attenuation is negligible compared to other uncertainties (antenna realization, external noise, and ionospheric variability); L_{wet} and L_{dry} are retained only for structural consistency with common link-budget bookkeeping [29,35–37].)

The transmit EIRP in dBm is

$$\text{EIRP}_{\text{dBm}} = P_{T_x,\text{dBm}} - L_{T_x} + G_{T_x}. \tag{4}$$

Using the dBm domain ($10\log_{10} k = -198.6$ dBm/K/Hz), the carrier-to-noise density and achieved energy-per-bit ratio are

$$\frac{C}{N_0} = \text{EIRP}_{\text{dBm}} - L_{\text{path}} + (G/T) + 198.6, \tag{5}$$

$$\left(\frac{E_b}{N_0}\right)_{\text{ach}} = \frac{C}{N_0} - 10\log_{10} R_b, \tag{6}$$

where R_b is the information bit rate (bit/s). If a mode is specified by a required SNR in bandwidth B, the equivalent requirement is

$$\left(\frac{E_b}{N_0}\right)_{\text{req}} = \text{SNR}_{\text{req}} + 10\log_{10}\left(\frac{B}{R_b}\right). \tag{7}$$

The minimum EIRP that closes the link (dBm) and the margin are

$$\text{EIRP}_{\text{min,dBm}} = \left(\frac{E_b}{N_0}\right)_{\text{req}} + 10\log_{10} R_b + L_{\text{path}} - (G/T) - 198.6, \tag{8}$$

$$\mathcal{M} = \text{EIRP}_{\text{dBm}} - \text{EIRP}_{\text{min,dBm}}. \tag{9}$$

For convenience, the corresponding satellite RF power that meets EIRP_{min} is obtained by inverting (4):

$$P_{T_x,\text{min,dBm}} = \text{EIRP}_{\text{min,dBm}} + L_{T_x} - G_{T_x}. \tag{10}$$

R_E is the mean Earth radius (km), h is the spacecraft altitude above the surface (km), and ε is the ground-station elevation angle (deg). $d_{\text{km}}(\varepsilon)$ is the slant range (km). f_{MHz} is the carrier frequency (MHz). L_{FS} is the free-space path loss (dB), and L_{path} is the total path loss including additional loss terms (dB). L_{pol} is the polarization mismatch loss, L_{wet} and L_{dry} are tropospheric attenuation bookkeeping terms, L_{ion} is an ionospheric loss allowance, and L_{pnt} is a pointing/pattern uncertainty allowance (all in dB). $P_{T_x,\text{dBm}}$ is transmitter RF output power (dBm), L_{T_x} is transmit-chain loss (dB), and G_{T_x} is transmit antenna gain (dBi). EIRP_{dBm} is effective isotropic radiated power (dBm). (G/T) is the receiver figure of merit (dB/K). k is Boltzmann's constant, and the constant 198.6 comes from $-10\log_{10} k$ in dB units. C/N_0 is the carrier-to-noise density (dB-Hz). E_b/N_0 is the energy-per-bit to noise-density ratio (dB). R_b is the information bit rate (bit/s), and B is the reference noise-equivalent bandwidth (Hz). $\mathcal{M}$ is the link margin (dB).

The waveform constants and detection thresholds adopted in Bid are summarized in Table 3. Although [1] specifies a 100 Hz reference bandwidth for CW, we adopt 500 Hz as a conservative worst case; the table reflects this choice, and the corresponding $(E_b/N_0)_{\text{req}}$ is obtained via (7) [30,32].

Table 3. Waveform constants and detection thresholds adopted in Bid [1].

Mode	R_b [bit/s]	Code Rate r	$\mathrm{SNR}_{\mathrm{req}}$ [dB]	B [Hz]	$(E_b/N_0)_{\mathrm{req}}$ [dB]
FT4	34.5	0.523	−17.5	2500	1.1
CW	16.67	1.000	−1.0	500	13.8

For the worst case at 5° and $h = 550$ km, evaluation of (2)–(3) gives

$$L_{\mathrm{path}}(28\ \mathrm{MHz}, 5^\circ) \approx 131.61\ \mathrm{dB}, \qquad L_{\mathrm{path}}(50\ \mathrm{MHz}, 5^\circ) \approx 136.61\ \mathrm{dB}.$$

Inserted in (8) and mapped to satellite RF output via (10), the minimum required Effective Isotropic Radiated Power (EIRP) and minimum required satellite transmit power at 5° with a closed link-budget at 0 dB margin are shown in Table 4.

Table 4. Bid worst-case link-budget closure (0 dB margin) at 5° elevation: minimum EIRP and satellite RF output power.

Mode & Band	$\mathrm{EIRP}_{\mathrm{min}}$ [dBm]	$P_{T_x,\mathrm{min}}$ [dBm]	$P_{T_x,\mathrm{min}}$ [mW]
FT4, 28 MHz	−25.51	0.00	1.00
FT4, 50 MHz	−20.51	5.00	3.20
CW, 28 MHz	−15.97	9.53	9.00
CW, 50 MHz	−10.97	14.53	28.4

At 28–50 MHz the effective system noise temperature at many receiving sites is often dominated by external contributions (galactic synchrotron emission and, depending on location, man-made noise), so (G/T) should be interpreted as a site-dependent effective figure of merit rather than a purely hardware-limited parameter [38,39]. In addition, ionospheric absorption (notably in the D region) can be non-negligible at these frequencies under some solar/geomagnetic conditions; this can be modeled as an added loss term beyond the small placeholder L_{ion} used here for bookkeeping [35]. To avoid overclaiming, we retain the nominal allowances in (3) for baseline closure and treat increased noise/absorption and antenna-pattern non-idealities via sensitivity analysis and (future) antenna/ground-station characterization.

Due to the non-ideal geometry and small satellite ground plane, the actual antenna gain can deviate significantly from theoretical estimates. Published small-satellite missions routinely report realized gains substantially lower than calculations, even after accounting for losses [40,41]. As a result, best practice is to treat analytical values as bounds and to replace them with electromagnetic simulation and/or prototype measurements for accurate link-budget assessment.

3.2. Initial Power Budget

This is a single-payload satellite. The main power consumers are the Sporadic-E beacon (RABSII, 300 mW) [1], the GNSS receiver (125 mW), and the communication system (500 mW electrical for 250 mW of Radio-Frequency (RF) power during transmission [42]. To avoid false positives in Es detections (e.g., the satellite being off but the ground station wrongly attributing a signal to Es), the payload beacon and the main transmitter may need to be enabled simultaneously during detection windows; operationally, this yields two relevant modes: a “science” (Es beacon) mode with potential co-transmit, and a “transmit-only” mode.

The component-level CBE for the system bus power, with solar generation regulated through an maximum power point tracking (MPPT) and DC–DC converters (assumed $\eta_{\mathrm{MPPT}} = \eta_{\mathrm{DC}} = 0.9$) is

$$P_{Transmit} = \frac{P_{\mathrm{RABSII}} + P_{\mathrm{GNSS}} + P_{\mathrm{COMMS}}}{\eta_{MPPT} \cdot \eta_{DC}} = \frac{300 + 125 + 500}{0.9 \cdot 0.9} = 1142 \text{ mW}. \quad (11)$$

For Bid (class I, first-of-a-kind), the contingency is taken as $C = 120\%$ from the stage-contingency table in [25]. Since there is currently one mode in this phase, using (12) and the maximum expected value (MEV) definition in (13),

$$CBE = max(P_{mode}) \quad (12)$$

$$MEV = (1 + C) \cdot CBE \quad (13)$$

the CBE and MEV sizing power at array level becomes

$$CBE_{Bid} = 1142 \text{ mW}, \;\; MEV_{Bid} = 2512 \text{ mW}$$

3.3. Initial Satellite Sizing

The satellite footprint is driven by an electronics area and solar-cell area, which cannot overlap on a given face. We adopt the PlanarSat packaging convention with a component packing factor κ_{pack} [26] and,

$$A_{\mathrm{electronics,tot}} = \kappa_{\mathrm{pack}} A_{IC} + A_{Payload} \quad (14)$$

At the Bid stage, only the payload electronics footprint (RABSII and its GNSS receiver) is known, whereas the platform electronics (OBC, EPS, ADCS, COMMS, etc.) is not yet defined. The area required for the platform electronics is therefore estimated by scaling the known payload electronics area by a factor κ, based on engineering judgement and experience with comparable small-satellite designs. In line with typical ratios, where platform electronics occupy on the order of twice the payload footprint, a value of $\kappa = 2$ is adopted.

RABSII is, at that time, targeted at a footprint of 42×42 mm^2, and it requires a GNSS receiver with a footprint of 25×35 mm^2. The payload electronics area is therefore

$$A_{\mathrm{payload}} = 42 \times 42 + 25 \times 35 = 1764 + 875 = 2639 \text{ mm}^2.$$

With $\kappa = 2$, the corresponding total electronics area at the Bid stage becomes

$$A_{\mathrm{electronics,tot_{Bid}}} = (1 + \kappa) A_{\mathrm{payload}} = 1764 + 875 + 2 \cdot (1764 + 875) = 7917 \text{ mm}^2 = 79.17 \text{ cm}^2.$$

This corresponds to approximately one third of the allocated electronics area being assigned to the payload and two thirds to the platform subsystems, which is considered a conservative but not excessively pessimistic assumption for a small satellite at this level of design maturity.

The total required active solar cell depends on MEV, solar irradiance at the mission altitude (low Earth orbit (LEO)), and the solar cell efficiency (η_{cell}):

$$A_{\mathrm{cell,tot}} = \frac{MEV}{I_{\mathrm{Solar},E}\, \eta_{\mathrm{cell}}} \quad (15)$$

Assuming AM0 irradiance $I_{\text{Solar},E} = 136.1\ \text{mW/cm}^2$ at LEO and $\eta_{\text{cell}} = 30\%$ [43], using Equation (15) the required active cell area is

$$A_{\text{cell,tot}_{\text{Bid}}} = \frac{2512\ \text{mW}}{136.1\ \text{mW/cm}^2 \times 0.30} = 61.55\ \text{cm}^2 \tag{16}$$

Solar cells are not 100% effective area, as they have an infill ratio specific to themselves:

$$A_{\text{cell,phys}_{\text{Bid}}} = \frac{A_{\text{cell,tot}}}{\eta_{\text{infill}}} \tag{17}$$

Using Equation (17), and considering an infill ratio of 0.9 (normal values range between 0.9 and 0.95),

$$A_{\text{cell,phys}_{\text{Bid}}} = \frac{61.55}{0.9} = 68.38\ \text{cm}^2$$

The final satellite size is the combination of the physical cell area and electronics area, where A_{Sat} is the minimum required area of a single face when both faces are fully utilized and there is no overlap between the solar cells and electronics:

$$A_{\text{Sat}_{\text{Bid}}} = \frac{A_{\text{electronics,tot}} + A_{\text{cell,phys}}}{2} \tag{18}$$

Using Equation (18), the minimum required footprint area of the satellite will be $A_{\text{Sat}_{\text{Bid}}} = 73.78\ \text{cm}^2$. The complete system is almost as big as a standard CubeSat subsystem which has approximately 81 cm^2 of the footprint area.

The quarter-wave radiator at 28 MHz is ∼2.5 m long, which is a dominant packaging and dynamics risk for a PlanarSat, and a primary driver of uncertainty in the effective realized gain G_{T_x} under free tumble. Accordingly, we treat G_{T_x} as a bounded realized parameter in the link budgets and plan engineering-model deployment tests and measured return-loss/pattern characterization prior to CDR (see Section 6).

In Figure 2, the conceptual PlanarSat as a result of the Bid phase is shown. The Bid phase shows that the FT4/CW beacon concept closes at 28/50 MHz under the adopted thresholds with batteryless, daylight-only operations. Power-first sizing (MEV ≈ 2.5 W) and no-overlap packaging imply a minimum single-face footprint of ∼74 cm^2, establishing the baseline for CoDR trades in array area, duty cycle, and mode scheduling.

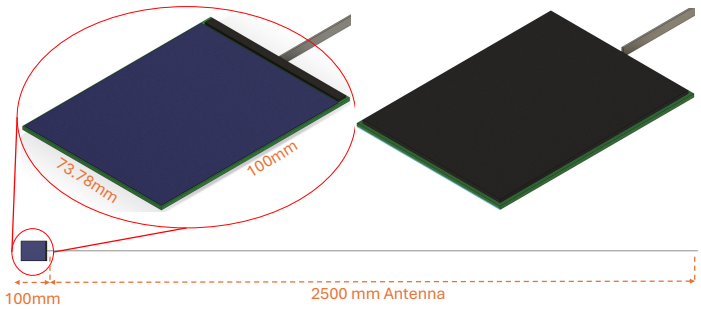

Figure 2. Bid conceptual PlanarSat with its quarter-wavelength 28 MHz antenna. The main body dimensions are 73.78 × 100 mm and antenna dimensions are 1 × 4 × 2500 mm. A zoomed-in main body image and full satellite view with its antenna are given together to visualize the scale.

4. Baseline Architecture—CoDR

The values calculated in Section 3, in combination with [1], support the conceptual feasibility of the mission under the stated RF/ground-segment and power-model assumptions; on-orbit demonstration and measured antenna/ground-station characterization remain required future validation steps.

A PocketQube-sized version of the RABSII payload is shown in Figure 3. This has been used in the baseline architecture for sizing and to visualize the satellite given in Section 4.3.

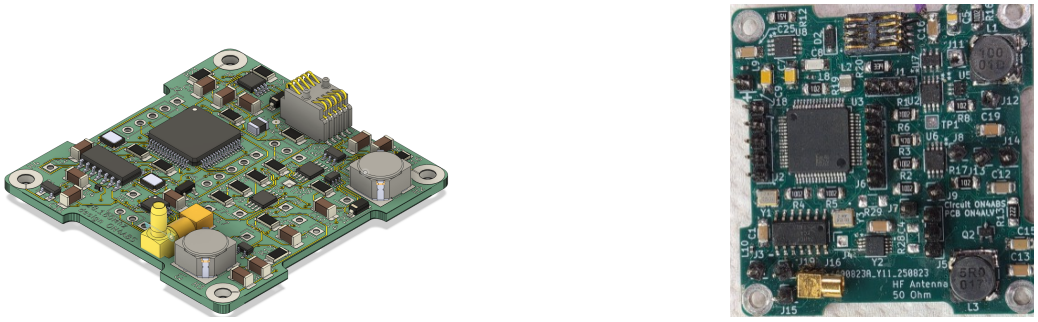

(**a**) RABSII design (**b**) Manufactured RABSII V6

Figure 3. RABSII, miniaturized to the PocketQube form factor, with a 50%-efficient onboard beacon, planned for Delfi-Twin mission [1,44].

The satellite employs STM32L4 family microcontrollers from STMicroelectronics [45] for the onboard computer and the communications subsystem. The communications system includes a Semtech SX1278 transceiver [46], a Qorvo SPF5043Z low-noise amplifier [47], and a Qorvo RFPA0133 power amplifier [48]. The electrical power system (EPS) comprises 3G30 solar-cell assemblies by AzurSpace [49], one MPPT circuit per cell based on the STMicroelectronics SPV1040 [50], and an STMicroelectronics STBB1-APUR adjustable-output DC–DC converter [51]. Additionally, the system includes a RAMXEED MB85RS4MTY Ferroelectric Random-Access Memory (FRAM) for data storage [52], and, for protection, an Analog Devices LTC4368-1 [53] and a Texas Instruments TPS3813 watchdog [54]. The physical footprints and nominal power consumption of these main components are summarized in Table 5. Flight heritage for the STM32L4 is documented in [55,56], and the remaining subsystems and components follow the PocketQube-class implementations reported in [42,57,58].

Table 5. Main components of the PlanarSat.

Component	Manufacturer	Area (mm^2)	Power (mW)
STM32L4 MCU	STMicroelectronics	196	P_{MCU} = 26
SX1278 Transceiver (RX/TX)	Semtech	36	P_{R_X} = 33 / P_{T_X} = 130
SPF5043 LNA	Qorvo	4.2	P_{LNA} = 230
RFPA0133 PA (20 dBm out)	Qorvo	9	P_{PA} = 420
SPV1040 MPPT	STMicroelectronics	13.2	0.26
STBB1-APUR DC–DC converter	STMicroelectronics	9	0.66
MB85RS4MTY FRAM	RAMXEED	30	P_{FRAM} = 14.4
LTC4368-1	Analog Devices	9	0.26
TPS3813-Q1 WD	Texas Instruments	7.8	P_{WD} = 0.5

The satellite operates in three modes: science, transmit, and standby. In science mode, the payload runs either autonomously or concurrently with the transceiver receive path to validate detections and suppress false positives. In transmit mode, the transceiver downlinks telemetry and buffered payload data. In standby mode, the spacecraft remains in a receive-only safe state awaiting ground commands. Mode transitions are managed by the on-board computer (OBC) in response to ground directives or time-tagged onboard sequences. The OBC, Transceiver (RX), and Transceiver (TX) each hosts its own microcontroller (MCU), which offloads processing from the OBC and enables a distributed architecture that reduces software complexity. The representative subsystem activity and power

states for each mode are summarized in Table 6. Science data are buffered in non-volatile memory during science mode and downlinked in transmit mode. These mode definitions and their duty cycles inform the spacecraft power budget and overall system sizing.

Table 6. Representative operational modes and active subsystems.

Mode	OBC	Payload	GNSS	Transceiver (RX)	LNA	Transceiver (TX)	PA	MPPT/Reg
Science	ON	ON	ON	ON	ON	OFF	OFF	ON
Transmit	ON	OFF	OFF	OFF	OFF	ON	ON	ON
Standby	ON	OFF	OFF	ON	ON	OFF	OFF	ON

In addition to the primary functions listed, supporting features such as fault protection, the watchdog (WD), and non-volatile FRAM are invoked by the flight software as required and may be active in any mode. Because the spacecraft can maintain core functionality without these features, and because their activation is orthogonal to the mode definitions, they are not itemized in Table 6.

4.1. Updated Link Budget

This phase builds on Bid and evaluates the link across the pass. Geometry is computed at each elevation sample (5°–90° in 5° steps) using Equation (1); the path term is $L_{\text{path}}(f, \varepsilon)$ from Equation (3). The satellite transmit chain remains $G_{T_x} = -25$ dBi and $L_{T_x} = 0.5$ dB; the ground station remains $G/T = -25$ dB/K. Performance is expressed in E_b/N_0 using Equation (6) with the information bit rate R_b. The FT4 and CW thresholds and rates in Table 3 (derived via Equation (7)) are applied directly.

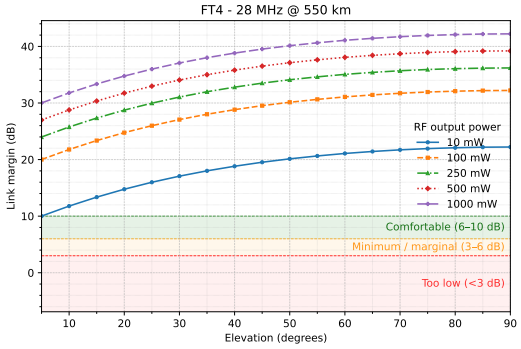

(**a**) Link Margin for FT4, 550 km Altitude, 28 MHz

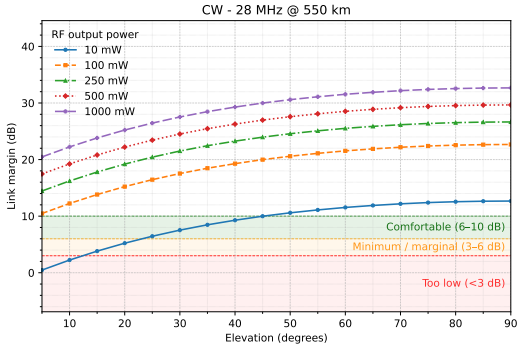

(**b**) Link Margin for CW, 550 km Altitude, 28 MHz

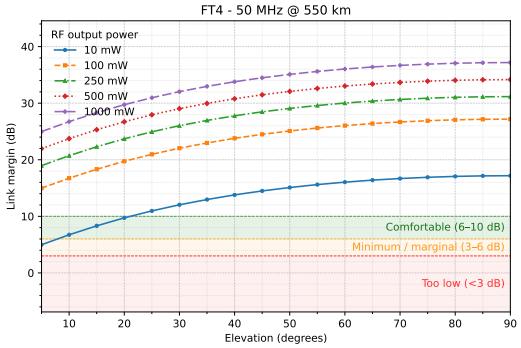

(**c**) Link Margin for FT4, 550 km Altitude, 50 MHz

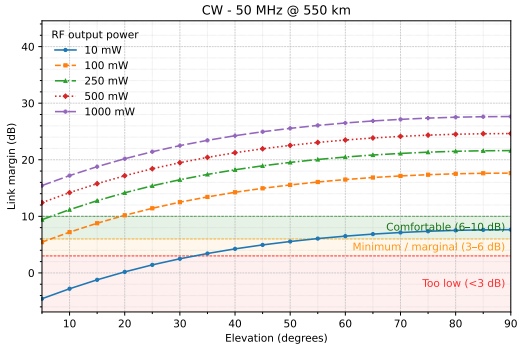

(**d**) Link Margin for CW, 550 km Altitude, 50 MHz

Figure 4. Link budget margins for FT4 [Data Rate: 0.0345 kbit/s, Code Rate: 0.523] and CW [Data Rate: 0.0167 kbit/s, Code Rate: 1.0]. (**a**) FT4 at 28 MHz. (**b**) CW at 28 MHz. (**c**) FT4 at 50 MHz. (**d**) CW at 50 MHz. Various agency recommendations are shown as patches in the graphs [59–61].

For each $f \in \{28, 50\}$ MHz, elevation $\varepsilon \in \{5°, 10°, 15°, 20°, \ldots, 85°, 90°\}$, and $P_{T_x} \in \{10, 100, 250, 500, 1000\}$ mW, we form $\mathrm{EIRP}_{\mathrm{dBm}}$ from Equation (4), compute C/N_0 from Equation (5), obtain $(E_b/N_0)_{\mathrm{ach}}$ from Equation (6), and report the margin $\mathcal{M}$ from Equation (9) using $\mathrm{EIRP}_{\mathrm{min,dBm}}$ from Equation (8). The transmit-power sweep is parametric to illustrate the trade space; the current baseline hardware selection targets 20 dBm (100 mW) RF output, and higher values are shown only to bound sensitivity should the measured G_{T_x} or site (G/T) require increased EIRP. Because $d(\varepsilon)$ in (1) decreases with elevation, L_{FS} in Equation (2) decreases and $\mathcal{M}$ increases with elevation for fixed P_{T_x}. For a fixed elevation, changing P_{T_x} shifts $\mathcal{M}$ one-for-one in dB. The resulting elevation-dependent margins for FT4 and CW, at both bands and for the five transmit-power cases, are shown in Figure 4.

The assumed transmit gain G_{T_x} represents an effective realized gain toward the ground station for a short, deployable HF radiator on a small ground plane [62], including mismatch and pattern non-idealities under free-tumble. The assumed (G/T) represents a mid-performance receiving site and antenna (highly variable across the amateur ecosystem due to sky noise and local man-made noise at 28–50 MHz) [38]. Because both quantities can deviate materially from their bounding values, Table 7 summarizes the resulting link-margin deltas and the transmit-power increase required to preserve the original margin. This sensitivity also bounds non-negligible HF/VHF-low effects such as additional ionospheric absorption and implementation losses that are not captured by the small fixed allowance in L_{ion} [63].

Table 7. Sensitivity of link margin $\mathcal{M}$ to transmit gain G_{T_x}, receiver figure of merit (G/T), and additional unmodeled losses L_{extra} (e.g., HF ionospheric absorption variability, pattern nulls, implementation losses). The margin change is $\Delta\mathcal{M} = \Delta G_{T_x} + \Delta(G/T) - L_{\mathrm{extra}}$. To preserve the original margin, transmit power must increase by $\Delta P_{T_x} = -\Delta\mathcal{M}$ (dB), i.e., a multiplicative factor of $10^{\Delta P_{T_x}/10}$.

Case	G_{T_x} [dBi]	(G/T) [dB/K]	L_{extra} [dB]	$\Delta\mathcal{M}$ [dB]	Power Factor
Baseline	−25	−25	0	0	1
Antenna worse by 5 dB	−30	−25	0	−5	3.16
Antenna worse by 10 dB	−35	−25	0	−10	10
Ground (G/T) worse by 5 dB	−25	−30	0	−5	3.16
Ground (G/T) worse by 10 dB	−25	−35	0	−10	10
Combined example	−35	−30	3	−18	63.1

A power factor greater than unity indicates the multiplicative increase in RF transmit power (or equivalently EIRP) required to preserve the same link margin under the specified degradation; it does not imply that bus power scales by the same factor once PA efficiency and duty cycle are accounted for.

In this early-phase analysis, we intentionally treat G_{T_x} and (G/T) as bounded, effective realized parameters rather than guaranteed design values. On the spacecraft side, the baseline radiator is a deployable HF quarter-wave element on a limited ground plane; therefore the assumed G_{T_x} will be replaced by measured matching efficiency and radiation pattern from an engineering model in a representative configuration prior to later design gates. On the ground side, EsTRACE relies on an opportunistic distributed receiver ecosystem rather than a dedicated, engineered ground-station network, so (G/T) varies significantly across sites at 28–50 MHz due to external noise and local interference [38]. Table 7 therefore bounds performance across plausible degradations, while a receiver-network-informed (G/T) characterization is retained as future work.

Various space agencies and standards generally recommend total link margins on the order of only a few decibels (3–6 dB) up to about 10 dB for LEO communication links [59–61,64]. For example, European Space Agency (ESA) recommends a system margin

of roughly 3–6 dB for LEO missions (with up to ∼10 dB for small satellites or uncertain ground station performance) [59,64], The National Aeronautics and Space Administration (NASA) guidelines typically cite 5–8 dB (increasing to 7–10 dB for CubeSat/smallsat missions to account for greater uncertainty) [60], and the American Institute of Aeronautics and Astronautics (AIAA)'s standard reference advises at least 3–6 dB (with 6–10 dB strongly advised for reliable links, especially for small satellites or in the presence of interference) [29]. Likewise, Japan Aerospace Exploration Agency (JAXA) generally allocates a total link margin of about 5–10 dB (including on the order of 1–3 dB for atmospheric/ionospheric effects, 2–4 dB for ground station and onboard hardware uncertainties, and 2–3 dB for manufacturing tolerances and aging) [61], and the ITU recommends a similar overall margin on the order of 6–10 dB for robust satellite link design [65]. Thus, the ≥5 dB link margins achieved in our PlanarSat design satisfy these typical requirements, providing a communications link budget buffer to ensure reliable performance.

4.2. Updated Power Budget

Systems and operating modes are defined in Tables 5 and 6. Per-mode CBE power is obtained by summing the electrical power of the subsystems active in that mode. Subsystems are grouped by functions and integrated circuits (ICs) as follows: the OBC comprises the MCU and WD; the RABSII beacon includes its own MCU and WD and a 50%-efficient beacon RF chain; the GNSS is a standalone module; the transmitter subsystem contains a dedicated MCU, WD, power amplifier (PA), and a transceiver IC; the receiver subsystem contains a dedicated MCU, WD, a receiver IC, and an low-noise amplifier (LNA). The MPPT and DC–DC regulators are applied only via their efficiencies (0.90 each) when converting array power to bus power [26].

Because the false-positive mechanism for Es detection is not yet fully characterized, it is unclear whether RABSII must co-transmit with the main transmitter during detection windows. Here, a "false positiv" refers to attributing a beacon non-detection (or anomalously weak reception) to Es-induced propagation loss when the spacecraft was in fact not transmitting due to power-aware gating, eclipse, or an operational inhibit. We therefore carry two alternatives into sizing: (i) RABSII+main transmitter concurrent ($P_{\mathrm{Sci+T_x}}$), and (ii) RABSII-only with deferred downlink (P_{Sci}); both cases are computed in the power and energy budgets, and the final operations policy is to be resolved in a later stage.

The mode power requirements are

$$P_{\mathrm{StandBy}} = \frac{\underbrace{P_{\mathrm{MCU}} + P_{\mathrm{WD}}}_{\mathrm{OBC}} + \underbrace{P_{\mathrm{MCU}} + P_{\mathrm{WD}} + P_{R_x} + P_{LNA}}_{\mathrm{Receiver}}}{\eta_{MPPT} \cdot \eta_{DC}}, \tag{19}$$

$$P_{\mathrm{Transmit}} = \frac{\underbrace{P_{\mathrm{MCU}} + P_{\mathrm{WD}}}_{\mathrm{OBC}} + \underbrace{P_{\mathrm{MCU}} + P_{\mathrm{WD}} + P_{T_x} + P_{PA}}_{\mathrm{Transmitter}}}{\eta_{MPPT} \cdot \eta_{DC}}, \tag{20}$$

$$P_{\mathrm{Sci}} = \frac{\underbrace{P_{\mathrm{MCU}} + P_{\mathrm{WD}}}_{\mathrm{OBC}} + \underbrace{P_{\mathrm{MCU}} + P_{\mathrm{WD}} + P_{\mathrm{Beacon}}}_{\mathrm{RABSII}} + P_{\mathrm{GNSS}} + \underbrace{P_{\mathrm{MCU}} + P_{\mathrm{WD}} + P_{R_x} + P_{LNA}}_{\mathrm{Receiver}}}{\eta_{MPPT} \cdot \eta_{DC}}, \tag{21}$$

and the false-positive-proof science mode with the main transmitter enabled is

$$P_{\mathrm{Sci+T_x}} = \frac{\underbrace{P_{\mathrm{MCU}} + P_{\mathrm{WD}}}_{\mathrm{OBC}} + \underbrace{P_{\mathrm{MCU}} + P_{\mathrm{WD}} + P_{\mathrm{Beacon}}}_{\mathrm{RABSII}} + P_{\mathrm{GNSS}} + \underbrace{P_{\mathrm{MCU}} + P_{\mathrm{WD}} + P_{T_x} + P_{PA}}_{\mathrm{Transmitter}}}{\eta_{MPPT} \cdot \eta_{DC}}. \tag{22}$$

In (21)–(22), the beacon DC power can be written from its RF setpoint as

$$P_{\text{Beacon}} = \frac{P_{\text{RF,Beacon}}}{\eta_{\text{RF,Beacon}}}, \qquad \text{e.g., } P_{\text{RF,Beacon}} = 100\ \text{mW},\ \eta_{\text{RF,Beacon}} = 0.5 \Rightarrow P_{\text{Beacon}} = 200\ \text{mW}, \tag{23}$$

consistent with the link margins in Figure 4 and the RABSII concept [1].

Substituting Table 5 values into (19)–(22) yields the bus–level CBE per mode: $P_{\text{StandBy}} = 390$ mW, $P_{\text{Transmit}} = 744$ mW, $P_{\text{Sci}} = 824$ mW, and $P_{\text{Sci+T}_x} = 1178$ mW.

At CoDR, for a class I satellite with power level below ∼1.2 W, the recommended contingency is $C = 105\%$ [25]. Using Equation (13), the satellite level sizing powers are

$$\begin{aligned} \text{MEV}_{\text{CoDR}}^{(\text{Sci})} &= (1 + 1.05)\, 824 = 1689\ \text{mW}, \\ \text{MEV}_{\text{CoDR}}^{(\text{Sci+T}_x)} &= (1 + 1.05)\, 1178 = 2415\ \text{mW}. \end{aligned} \tag{24}$$

As the solar array is sized by the largest credible operational case and operations are not yet finalized, both $\text{MEV}_{\text{CoDR}}^{(\text{Sci})}$ and $\text{MEV}_{\text{CoDR}}^{(\text{Sci+T}_x)}$ are retained for downstream area and energy sizing.

4.3. Updated Satellite Sizing

The electronics area is computed from the detailed CoDR parts list using (14). The GNSS and RABSII are complete modules and are counted as $A_{Payload} = 4800\ \text{mm}^2$. The remaining ICs, including their passives/routing as captured in the preliminary board placement, occupy $A_{\text{electronics}} = 757.75\ \text{mm}^2$. We apply $\kappa_{\text{pack}} = 4$, as only bare IC footprints are known and peripherals are not yet chosen [26]. Hence

$$A_{\text{electronics,tot}_{CoDR}} = 4 \times 757.75 + 4800 = 7831\ \text{mm}^2 = 78.31\ \text{cm}^2.$$

The array is sized per operational mode using the CoDR MEV values and the photovoltaic relations (15)–(17). With $I_{\text{Solar},E} = 136.1\ \text{mW/cm}^2$ and a 29.3% AZUR cell assembly [49],

$$\begin{aligned} A_{\text{cell,tot}_{\text{CoDR}}}^{\text{Sci}} &= \frac{1689\ \text{mW}}{136.1\ \text{mW/cm}^2 \times 0.293} = 42.35\ \text{cm}^2, \\ A_{\text{cell,tot}_{\text{CoDR}}}^{\text{Sci+T}_X} &= \frac{2415\ \text{mW}}{136.1\ \text{mW/cm}^2 \times 0.293} = 60.56\ \text{cm}^2. \end{aligned}$$

Applying the tile packing factor $\eta_{\text{infill}} = 0.94$,

$$A_{\text{cell,phys}_{\text{CoDR}}}^{\text{Sci}} = \frac{42.35}{0.94} = 45.05\ \text{cm}^2, \tag{25}$$

$$A_{\text{cell,phys}_{\text{CoDR}}}^{\text{Sci+T}_x} = \frac{60.56}{0.94} = 64.43\ \text{cm}^2. \tag{26}$$

Under the no-overlap, two-face utilization assumption (18), the minimum single-face areas are

$$A_{Sat_{\text{CoDR}}}^{\text{Sci}} = \frac{78.31 + 45.05}{2} = 61.68\ \text{cm}^2$$

$$A_{Sat_{\text{CoDR}}}^{\text{Sci+T}_x} = \frac{78.31 + 64.43}{2} = 71.37\ \text{cm}^2$$

In both cases, solar cells fit on one face with margin for harness and keep-outs. The difference between the two configurations arises from the different MEVs which requires a different solar array size. Figure 5 shows the satellite sized for $A_{\text{CoDR}}^{\text{Sci+T}_x}$, with the solar cells and a small remaining portion of electronics placed on one face and rest of the electronics placed on the opposite side.

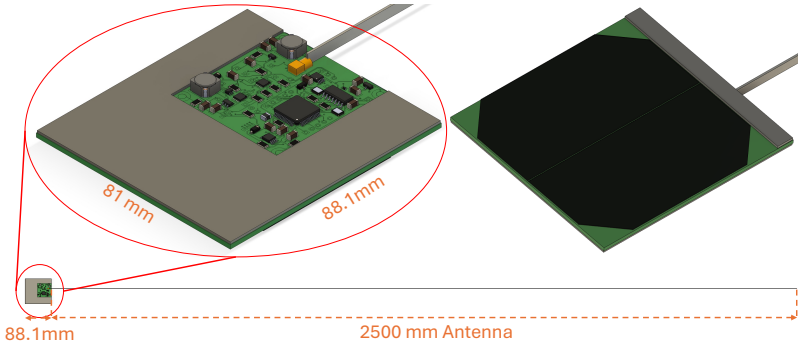

Figure 5. CoDR architecture of the PlanarSat with its quarter-wavelength 28 MHz antenna. Main body dimensions are 81 × 88.1 mm and antenna dimensions are 1 × 4 × 2500 mm. The zoomed-in main body image and full satellite view with its antenna are given together to visualize the scale. RABSII is placed in the middle, and gray boxes are placeholders for other ICs/electronics.

CoDR fixes the component set and mode definitions and updates the budgets: the computed link margins meet the recommended few-to-10 dB ranges, per-mode bus CBE spans 390–1178 mW, and the PlanarSat footprint closes in ∼62–71 cm^2 (Science vs. Science+Tx). Both alternatives are retained for PDR, providing a concrete baseline for verification and operations policy.

5. Preliminary Design—PDR

Following CoDR, the nominal concept-of-operations time multiplexes the payload beacon and the main telemetry transmitter (i.e., no nominal simultaneous operation). The main transmitter is enabled only when the onboard instantaneous power margin, computed from measured array power and bus consumption, exceeds a threshold defined in the OPE [25,26]. However, analysis will still be conducted for Science+Transmission to check the feasibility of such operations with the final configuration. For clarity, we retain the Sci+Tx case throughout this paper as a conservative upper-bound (maximum instantaneous-load) and as an optional contingency, should later false-positive-mitigation trades motivate concurrent beacon+telemetry operation; it is not required by the nominal PDR schedule. To support this closed-loop decision at PDR, two power-management functions are added: (i) bus-voltage and shunt-sense current monitoring using the Texas Instruments INA226 to estimate generation and load in real time [66]; and (ii) protected high-side power distribution using the TI TPS255x family to selectively enable the payload, receiver, and transmitter and to enforce per-line current limits during fault isolation [67]. All other subsystem selections remain as in CoDR.

The RABSII payload concept and waveform choices are unchanged from CoDR: sequential FT4 and continuous-wave (CW) beacons at 28 MHz and 50 MHz, time-aligned to GNSS, and intended for reception by the amateur ecosystem [1,14,30,32]. The baseline on-air schedule is a 30 s FT4 period followed by a 30 s CW period, repeated, with the option to interleave or pause either stream from the ground. GNSS pulse per second (PPS) is required continuously for slotting; National Marine Electronics Association (NMEA) messages and coordinates are consumed at 1 Hz by the payload controller.

Because the bus has no energy storage and no attitude determination and control system (ADCS), brownout or blackout risk depends on orientation, orbit location, and instantaneous load. At PDR, two array/electronics layout options are therefore carried forward for comparison: a separated architecture (MEV_{PDR} cells on one face, electronics on the opposite face) and a mixed architecture (MEV_{PDR} cells on both faces with the electronics split). Simulations using these options are provided in the following subsection.

5.1. Changes in PDR

The satellite houses additional components with respect to CoDR, five INA226 devices and four TPS255x devices: three TPS2553 (active-high enable) allocated to GNSS, RABSII, and the transmitter, and one TPS2552 (active-low enable) for the receiver. A single INA226 consumes 1.09 mW with a 14.7 mm^2 footprint; a single TPS255x consumes at most 0.25 mW with a 4.64 mm^2 footprint.

For the link budget, the ground-station parameters and the satellite antenna gain are treated as bounding values at PDR. The antenna will be fabricated and measured, and the matching circuitry completed so that measured characteristics replace these bounds and a single radiator can be used for all required operations.

5.1.1. Power Budget

Electronics are largely unchanged; the additional components are added to the summation on the right-hand side of Equation (21) as $5 \times P_{\text{INA}} + 4 \times P_{\text{TPS255x}}$. Both functions operate at 3.3 V. The added power is 6.45 mW. Including these contributions, the current-best estimate for the highest power consuming mode (Science) is $CBE_{\text{PDR}} = 832$ mW. Using Equation (13) for a Class-I satellite in the 0 to 1.2 W regime at PDR, the recommended contingency factor is $C = 70\%$, yielding [25]

$$MEV_{\text{PDR}} = 1.70 \times CBE_{\text{PDR}} = 1414 \text{ mW}$$

In CoDR, the baseline selects two Azur solar cells that generate 2422 mW at 0° sun incidence. Maintaining the same array sizing for PDR gives $MPV_{\text{PDR}} = 2422$ mW. The available margin is

$$\Delta P_{\text{Margin}} = MPV_{\text{PDR}} - MEV_{\text{PDR}} = 2422 \text{ mW} - 1414 \text{ mW} = 1008 \text{ mW}.$$

5.1.2. Satellite Sizing

The total electronics area increases with the new components. Using Equation (14), the PDR electronics area is

$$A_{\text{electronics,tot}_{PDR}} = 4 \times 849.81 + 4800 = 8199.24 \text{ mm}^2 = 82 \text{ cm}^2.$$

Two bus configurations are evaluated, differing only in how much photovoltaic area is instrumented relative to MEV:

- Single-sided array: cells are placed on one face, and the opposite face hosts the electronics.
- Two-sided array: cells are placed on both faces, with the electronics split across the two faces.

Assuming either two cells on one face or two cells on each face (one cell has 32.11 cm^2 physical area with a 0.94 infill ratio [49]), the total instrumented cell area is

$$A_{\text{cell,phys}} = \begin{cases} 64.22 \text{ cm}^2 & \text{single-sided (2 cells total)}, \\ 128.44 \text{ cm}^2 & \text{two-sided (4 cells total)}. \end{cases}$$

For the separated architecture (all solar cells on one face and all electronics on the opposite face), the required single-face footprint is set by the larger of the two per-face allocations:

$$A_{Sat_{\text{PDR}}}^{\text{Separated}} = \max\left(A_{\text{electronics,tot}_{\text{PDR}}}, A_{\text{cell,phys}}\right) = \max(82, 64.22) = 82 \text{ cm}^2.$$

For the mixed architecture (cells on both faces with electronics split across both faces), the minimum single-face footprint under the no-overlap assumption is

$$A_{Sat_{\mathrm{PDR}}}^{\mathrm{Mixed}} = \frac{A_{\mathrm{electronics,tot_{PDR}}} + A_{\mathrm{cell,phys,tot}}}{2} = \frac{82 + 128.44}{2} = 105.22\ \mathrm{cm}^2.$$

PDR phase satellite is shown in Figure 6. Simulations based on the PDR satellite combination with power values are provided in the next subsection.

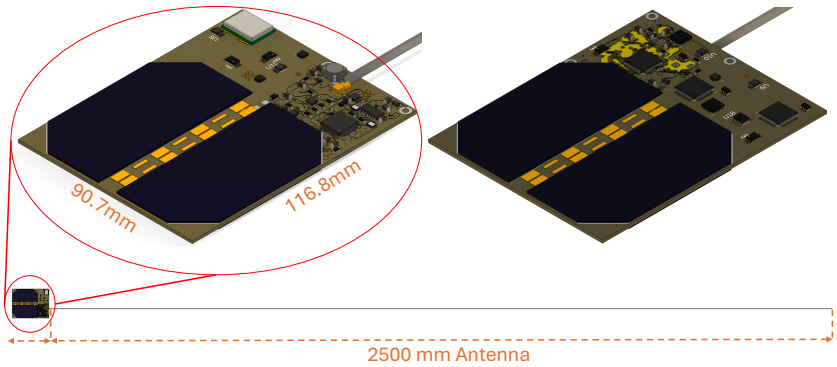

Figure 6. PDR architecture of the PlanarSat with its quarter-wavelength 28 MHz antenna. The main body dimensions are 90.7 × 116.8 mm, and the antenna dimensions are 1 × 4 × 2500 mm. A zoomed-in main body image and full satellite view with its antenna are given together to visualize the scale. RABSII is placed in the middle, and gray boxes are placeholder for other ICs/electronics.

5.2. Operational Envelope and Simulations

Continuous operation for a mode with demand $\mathrm{CBE_{PDR}}$ requires

$$\theta_{\max}(Mode) = \arccos\left(\frac{\mathrm{CBE}_{\mathrm{PDR}}^{\mathrm{mode}}}{MPV_{\mathrm{PDR}}}\right). \tag{27}$$

Using the current best estimate values; $\mathrm{CBE}_{PDR}^{\mathrm{Sci+T_x}} = 1186$ mW, $\mathrm{CBE}_{PDR}^{\mathrm{Sci}} = 832$ mW, $\mathrm{CBE}_{PDR}^{\mathrm{Transmit}} = 752$ mW, $\mathrm{CBE}_{PDR}^{\mathrm{StandBy}} = 398$ mW and the satellite highest generation capability MPV = 2422 mW, the resulting angles are

$$\begin{aligned}
\theta_{\max}(\mathrm{Sci} + \mathrm{T_x}) &= \arccos\left(\frac{1186}{2422}\right) = 60.6^\circ \\
\theta_{\max}(\mathrm{Sci}) &= \arccos\left(\frac{832}{2422}\right) = 69.9^\circ \\
\theta_{\max}(\mathrm{Transmit}) &= \arccos\left(\frac{752}{2422}\right) = 71.9^\circ \\
\theta_{\max}(\mathrm{StandBy}) &= \arccos\left(\frac{398}{2422}\right) = 80.5^\circ
\end{aligned}$$

These are the maximum deviations from normal incidence at which the satellite can continuously support transmission and payload modes without energy storage or sun-pointing.

To place these envelopes in context, we propagate the nominal orbit for 2 days with a 0.25 s step size in MATLAB's (version:R2025a) `satelliteScenario` using a two-body Keplerian propagator. Rather than reproducing a specific launch window, we assume a representative mid-morning sun-synchronous orbit with a 10:30 a.m. local time descending node, as commonly used for Earth-observation missions. This choice fixes the relative

orientation between the orbital plane and the sun and can be represented by a right ascension of the ascending node of $\Omega = 212.1^\circ$ at an arbitrary reference epoch.

For the power-envelope analysis, only the sun-orbit geometry (through the evolution of the β-angle and eclipse durations) is relevant; a uniform rotation of the RAAN or a shift in epoch does not change these quantities but only re-phases them in time. The remaining orbital parameters at the reference epoch are

$$a = 6922.7 \text{ km}, \ e = 0.00104, \ i = 97.4799^\circ, \ \omega = 177.2905^\circ, \ \nu = 182.8386^\circ.$$

Figures 7 and 8 use a greedy operating-mode assignment. At each time sample, the spacecraft is placed in the most power-demanding mode that the instantaneous array power can support, in the priority order Sci+Tx > Sci > Tx > Standby. Because the PDR nominal operations time-multiplex beacon and telemetry, any time tagged "Sci+Tx" in Figures 7–9 should be interpreted as power headroom sufficient for concurrent operation if enabled; under the nominal policy those intervals would be partitioned between Sci and Tx rather than being executed concurrently. Consequently, the reported mode fractions indicate the fraction of time actually spent in each primary operating mode under this rule, not the broader fraction of time during which a lower-power mode would have been feasible. For example, whenever Sci+Tx is feasible, that interval is counted under Sci+Tx rather than under Sci or Standby.

In the propagation shown in Figure 7, the single-face case spends approximately 35% of the orbit in eclipse, 15% in sunlit conditions where the array is not illuminated, and 5% with insufficient power for any of the listed modes. Among the operating modes, the minimum time allocations implied by the greedy selection are 5% Standby, 5% Science, 2% Transmission, and 30% Science+Transmission. These percentages reflect the time assigned to the highest feasible mode and therefore represent lower bounds for the less demanding modes. Percentages may not sum exactly due to rounding and the classification rule.

In the propagation shown in Figure 8, the case spends approximately 35% of the orbit in eclipse and 15% with insufficient power for any of the listed modes. The resulting minimum time allocations for the operating modes are 10% Standby, 8% Science, 4% Transmission, and 30% Science+Transmission. As above, these are the times selected by the greedy assignment for the highest feasible mode at each instant; values may not sum exactly due to rounding and the classification rule.

Both simulations use a deterministic reference attitude history (nadir-pointing body frame) to generate a repeatable sun-incidence time history and to visualize the greedy power-aware mode selection. This is not intended as a prediction of the free-tumbling attitude; the isotropic-tumble bound in the next subsection provides an attitude-agnostic sunlit availability estimate. Under that assumption, the mixed architecture may not appear advantageous in the greedy tally; however, it is more tolerant to attitude flips or illumination disturbances because at least one surface can still generate power when the other is unfavorable. In practice, real attitude motion and small disturbances will perturb the sun incidence and shift time from higher-power to lower-power modes. With no energy storage, these excursions can produce brief brownouts; conversely, architectures that sustain partial illumination more often reduce the risk of brownout and increase on-air availability.

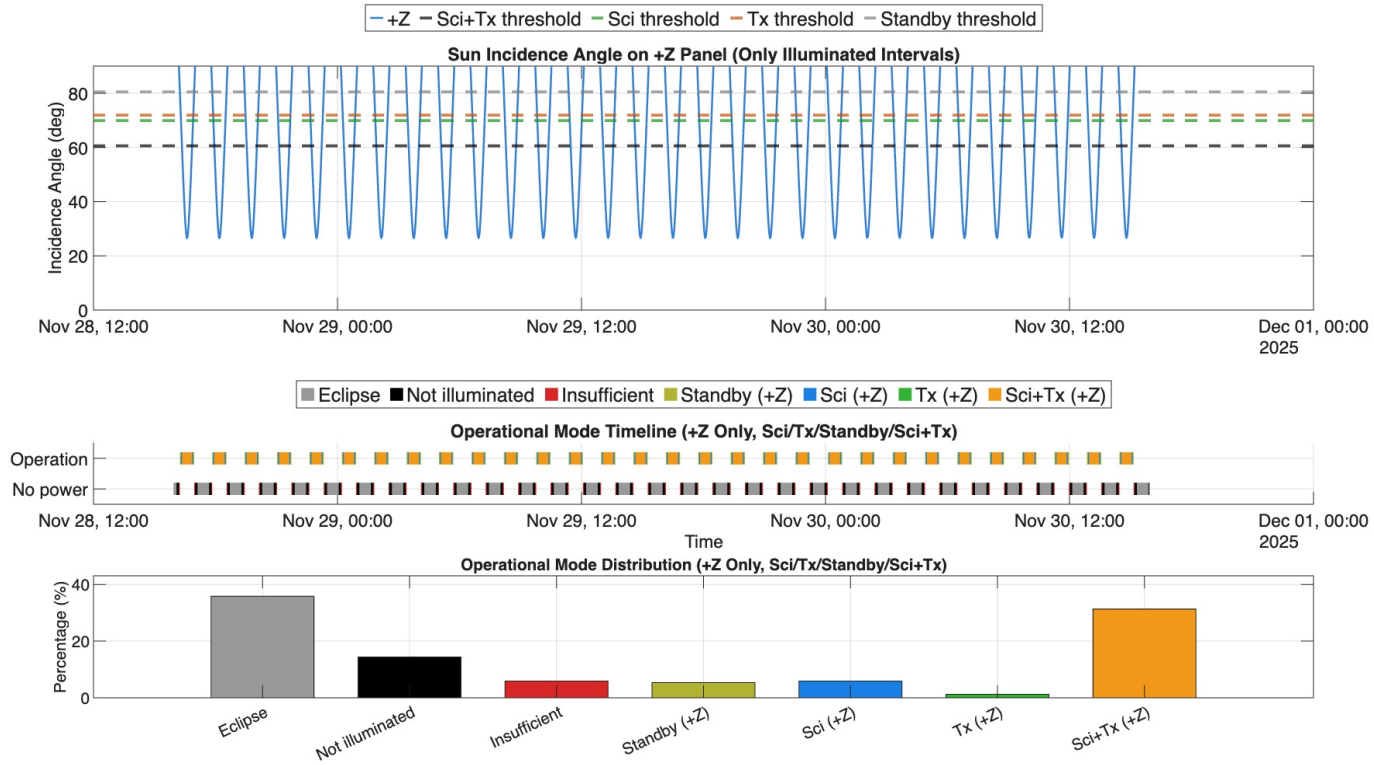

Figure 7. EsTRACE (PlanarSat) operational power-envelope simulation for the separated architecture (solar cells on the $+Z$ face only; electronics on the opposite face), using a direct-sun cosine-incidence model with no energy storage. **Top:** Sun-incidence angle θ on the $+Z$ solar-array face during illuminated intervals ($\theta = 0^\circ$ is normal incidence; larger θ reduces instantaneous generation). The horizontal dashed lines are the per-mode incidence limits $\theta_{\max}$ from Equation (27); when θ rises above a mode's dashed line, the instantaneous array generation is insufficient to sustain that mode in a batteryless system, so the spacecraft must fall back to a lower-power mode. **Middle:** Mode selected by the greedy, power-aware scheduler over the full timeline (priority order Sci+Tx $\rightarrow$ Sci $\rightarrow$ Tx $\rightarrow$ Standby), with eclipse and sunlit-but-unilluminated intervals (sun incident on the opposite face) shown explicitly. **Bottom:** Fraction of the total simulation time assigned to each state/mode under this greedy policy (lower-power modes are under-counted whenever a higher-power mode is feasible).

Analytical Isotropic-Tumble Bound (Sunlit Fraction)

To complement the time-history simulations (which assume a specific attitude history), we provide a conservative analytical bound on sunlit mode availability for a free-tumbling, batteryless PlanarSat under an isotropic attitude model. Let $u = \cos\theta$ be the direction cosine between the sun vector and the solar-array normal. For an isotropically distributed body normal, u is uniformly distributed on $[-1, 1]$ [68]. Using the standard direct-sun cosine-incidence model for photovoltaic generation (albedo neglected; no energy storage), the instantaneous available electrical power scales with the projected area [29]: for a single-sided array (separated architecture) $P_{\text{gen}} = MPV \cdot \max(0, u)$, and for the two-sided array option considered here (equal solar-cell allocation on both faces, so either illuminated face can deliver MPV at $\theta = 0^\circ$) $P_{\text{gen}} = MPV \cdot |u|$. A mode with demand P_{mode} is supportable in sunlight when $P_{\text{gen}} \geq P_{\text{mode}}$, i.e., when $u \geq x$ (single-sided) or $|u| \geq x$ (two-sided), where $x = P_{\text{mode}}/MPV$. Because u is uniform on $[-1, 1]$, these conditions yield closed-form sunlit availability fractions:

$$f_{\text{single}}(x) = \frac{1 - x}{2}, \qquad f_{\text{two}}(x) = 1 - x, \qquad 0 \leq x \leq 1. \tag{28}$$

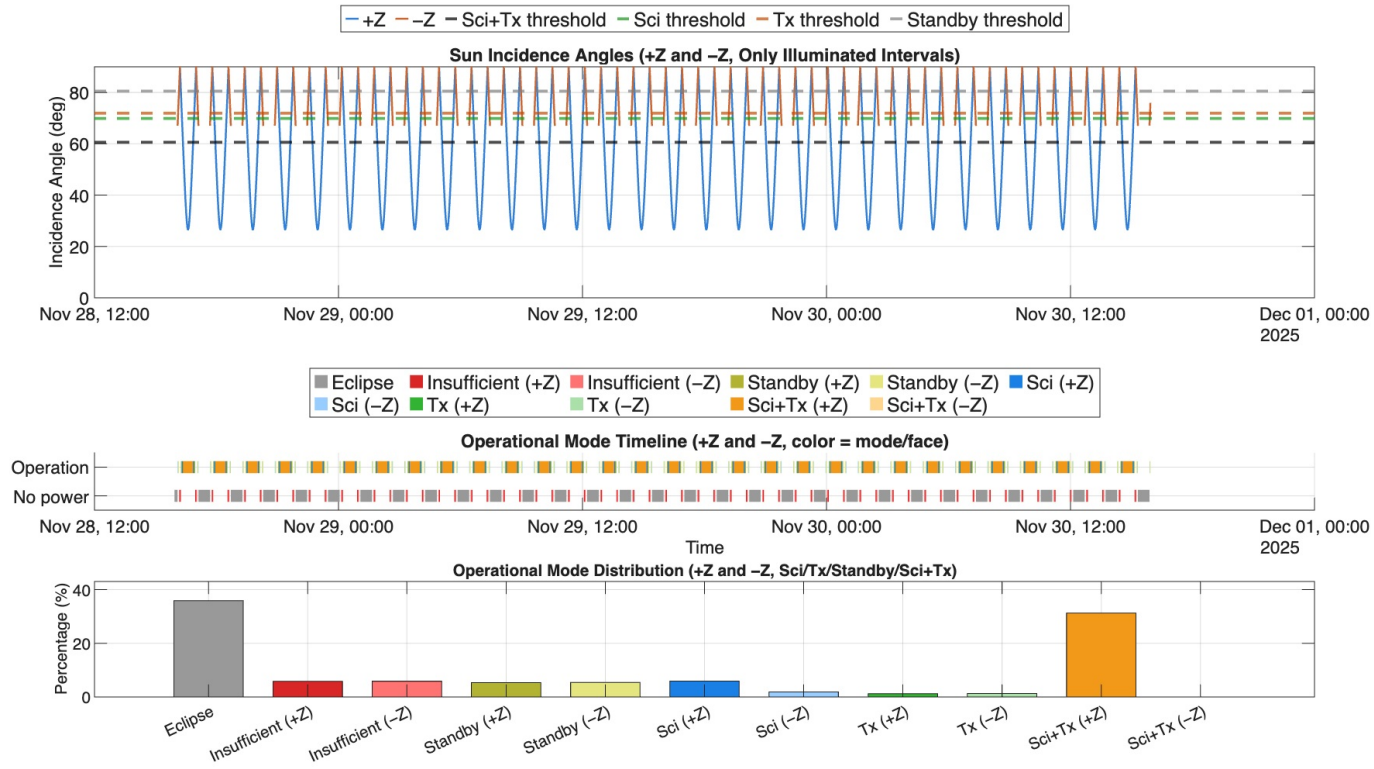

Figure 8. EsTRACE (PlanarSat) operational power-envelope simulation for the mixed architecture (solar cells on both $+Z$ and $-Z$ faces, enabling power generation under attitude flips), using a direct-sun cosine-incidence model with no energy storage. **Top:** Sun-incidence angles θ_{+Z} and θ_{-Z} for the two solar-array faces, shown only over the time intervals when the corresponding face is illuminated. The horizontal dashed lines are the per-mode incidence limits $\theta_{\max}$ from Equation (27); when the illuminated face's incidence exceeds a mode's dashed line, that mode cannot be sustained on instantaneous solar power and the scheduler must drop to a lower-power mode. **Middle:** Greedy, power-aware mode schedule over time, with color encoding both the selected operating mode and which face ($+Z$ or $-Z$) was illuminated while that mode executed. **Bottom:** Fraction of the total simulation time spent in each state, resolved by mode and illuminated face.

Table 8 reports these bounds for the PDR mode powers and $MPV_{\mathrm{PDR}} = 2422\,\mathrm{mW}$. These values ignore eclipse and therefore bound only the sunlit portion of the orbit.

Table 8. Analytical isotropic-tumble bound on sunlit mode availability (ignoring eclipse) for PDR. Here $x = P_{\mathrm{mode}}/MPV$ and f is the fraction of isotropic sunlit attitudes that satisfy $P_{\mathrm{gen}} \geq P_{\mathrm{mode}}$.

Mode	$x = P_{\mathrm{mode}}/MPV$	$f_{\mathrm{single}} = \frac{1-x}{2}$	$f_{\mathrm{two}} = 1 - x$
Sci+Tx	$1186/2422 = 0.49$	0.26	0.51
Sci	$832/2422 = 0.34$	0.33	0.66
Transmit	$752/2422 = 0.31$	0.35	0.69
Standby	$398/2422 = 0.16$	0.42	0.84

Figure 9 repeats the mixed-architecture run but adds a small pointing jitter to the sun-panel incidence at each simulation step when the spacecraft is not in eclipse. At every step one random off-pointing angle is drawn with zero mean and a chosen 1-sigma width of 3 deg and that same offset is applied to all faces, representing a brief whole-body attitude error rather than panel-specific flexing. Angles are then limited to their physical range, and any face with a grazing or night-side incidence produces no power. Instantaneous face powers and the total array power are recomputed with this disturbed incidence, while the mode-selection priority remains unchanged. The effect is most visible for samples that sit close to a mode threshold in the undisturbed case: small perturbations nudge those

samples above or below the boundary, which breaks longer high-power segments into shorter bursts and produces brief dropouts when no energy storage is available. Deeply illuminated or fully dark samples are largely unaffected. This figure is intended to illustrate the continuity and robustness of the schedule in the presence of small realistic attitude errors; it is not a re-estimation of the aggregate mode time budgets reported for the undisturbed runs.

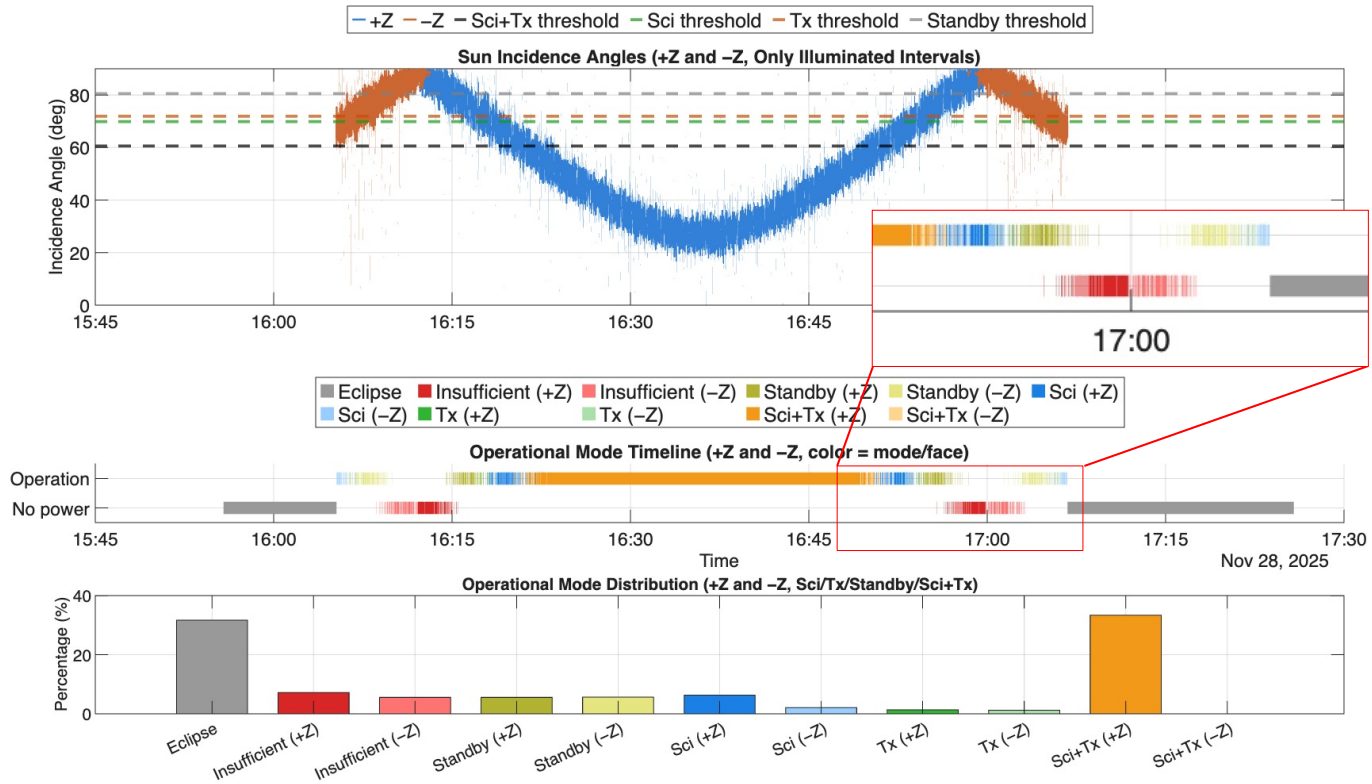

Figure 9. EsTRACE (PlanarSat) operational power-envelope simulation for the mixed (two-sided array) architecture with a small stochastic incidence disturbance applied in sunlight (batteryless, direct-sun cosine-incidence model). **Top:** Sun-incidence angles on the $+Z$ and $-Z$ faces (shown only during illuminated intervals). Horizontal dashed lines are the per-mode incidence limits $\theta_{\max}$ from Equation (27); excursions above a threshold imply insufficient instantaneous generation to sustain that mode. **Middle:** Greedy, power-aware mode schedule (Sci+Tx $\rightarrow$ Sci $\rightarrow$ Tx $\rightarrow$ Standby), color-coded by mode and illuminated face. A zoomed-in portion shows disturbance-driven mode changes as a reflection of power fluctuations around the mode thresholds. **Bottom:** Fraction of total time assigned to each state/mode under the greedy policy. The red zoom inset highlights how small incidence fluctuations near $\theta_{\max}$ thresholds can trigger rapid switching between adjacent modes in a batteryless system (mode "chatter" near boundaries).

6. Results and Future Work

Figure 10 shows the maximum power capability carried at each phase and how it is used for sizing. The current best estimate CBE is the bus power computed from the component list and mode definitions. Applying the phase-appropriate contingency yields the MEV. The maximum possible value (MPV) is the on-orbit cap used for hardware selection and tiling. At Bid no additional margin is defined, so MPV equals MEV. At CoDR the margin above MEV is limited by the available commercial solar-cell formats. At PDR the CoDR sizing is retained but the cell allocation is changed, which creates a margin above MEV determined by the available tile geometry.

The same power-first method is applied across Bid, CoDR, and PDR. Per-mode bus CBE power is derived from the component list, contingency converts CBE to MEV, and MEV is mapped to required active cell area using the adopted cell efficiency and AM0 irradi-

ance [25,26]. For PlanarSat packaging, the single-face footprint follows the no-overlap rule between electronics and cells [16].

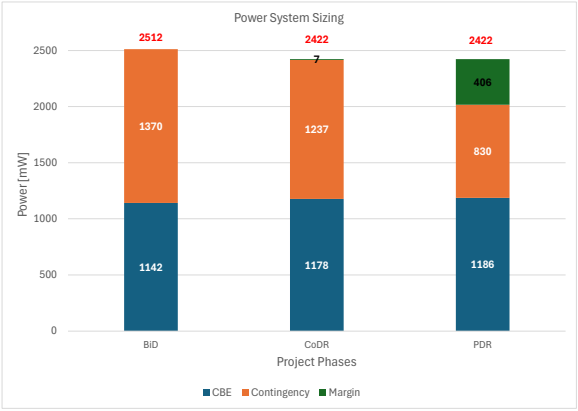

Figure 10. Power-system sizing evolution across BiD, CoDR, and PDR. For each phase, the stacked bar shows the worst-case per-mode bus CBE (blue) and the phase-appropriate contingency addition (orange), whose sum is the MEV (MEV = CBE $(1 + C)$). The green segment shows the additional headroom between MEV and the selected solar-array maximum available power MPV at $\theta = 0^\circ$ incidence (direct-sun model; no albedo). The red marker/value at the top of each bar indicates MPV. At BiD, MPV = MEV (no added headroom), while at CoDR/PDR MPV is limited by discrete commercial solar-cell tiling formats and retained to support the batteryless operational envelope analysis.

Table 9 summarizes the evolution. Bid uses the science plus main-transmission case with class-I contingency for concept feasibility. From Bid to CoDR the main improvement comes from explicit mode decomposition and part selection, which reduces the science MEV and the required cell area. CoDR carries both science and science plus transmit alternatives. PDR changes the array allocation rather than parts. Two-sided tiling redistributes the same MPV across faces to reduce incidence sensitivity without energy storage. The added monitors and protected switches slightly increase standby draw but enable power-aware scheduling; they do not change the beacon concept [1]. The system remains feasible in a PlanarSat envelope, which confirms that power and surface area, not mass, govern feasibility for this class [16].

Table 9. Evolution of key power-sizing quantities across design phases. MEV values include contingency as defined in [25]. $A_{\text{cell,tot}}$ denotes the total solar-cell area installed on the spacecraft, while A_{Sat} is the projected single-face satellite area. For two-sided configurations, the total cell area increases because both faces are populated with solar cells, but the MPV (maximum power available at any given instant) remains unchanged since only one face is illuminated by the sun at a time (albedo neglected).

Phase and Configuration	Bus CBE [mW]	MEV [mW]	MPV [mW]	$A_{\text{cell,tot}}$ [cm^2]	A_{Sat} [cm^2] Single Face
Bid science (single-sided)	1142	2512	2512	68.38	73.78
CoDR science (single-sided)	824	1689	2422	45.05	61.68
CoDR science+Tx (single-sided)	1178	2415	2422	64.43	71.37
PDR science (one-sided)	832	1414	2422	64.22	82.00
PDR science (two-sided)	832	1414	2422	128.44	105.22
PDR science+Tx gated (two-sided)	1186	2016	2422	128.44	105.22

For the same instantaneous MPV, a two-sided allocation reduces sensitivity to sun incidence and produces a wider operational power envelope under free tumble. In practice, the selected two-sided total area is set so that the PDR envelope in Figure 8 is met at the chosen MPV, subject to tiling keep-outs and harness constraints.

Future Work

Before the Critical design review (CDR) the following items will be closed to turn the PDR baseline into a flight-ready configuration.

- Packaging and envelope. Finalize the outline and keep-outs to fit a standard PocketQube or CubeSat deployer, including mounting points, access for remove before flight (RBF), and separation-switch locations. Confirm harness routing and connector clearances in the stowed configuration and freeze mass properties for provider reviews.
- Antenna system. Complete the radiator geometry and placement for the beacon and telemetry bands, including folded length, hold-down, and release. Design and verify the matching network so that a single radiator can support all required modes. Fabricate an engineering model and measure return loss, radiation pattern, and efficiency in a representative ground plane to replace the bounding values used in the link budget.
- Inhibit and safety chain. Define the RBF, deployment switches, and the inhibit switches they control, consistent with deployer and launch-provider requirements. Verify the power-up sequence and safe states for integration, launch, and early orbit.
- Operational power envelope in hardware. Implement power-aware scheduling on the OBC and verify it with a solar-array emulator and programmable loads. Inject small incidence jitter and show that mode transitions follow the PDR rule.
- Thermal analysis. Complete steady-state and transient thermal balance for hot and cold cases, including temperature-dependent cell efficiency and converter performance. Identify any required coatings or radiator areas.
- Structural and vibration. Run the vibration simulation to define test levels and notching. Manufacture the structural model and complete sine, random, and shock tests. Update fastener torque, stowage, and hold-down details from test outcomes.
- RF end-to-end and ground segment. Calibrate the transmit chain at the intended setpoints and verify spectral masks and timing for the selected waveforms. Measure antenna return loss, efficiency, and pattern to replace bounded G_{T_x} values. Characterize the effective (G/T) distribution of representative receiving sites at 28/50 MHz (including external-noise conditions per ITU-R P.372) to refine detection probability and link closure margins.
- Constellation operations and interference management. Define a channelization plan (GNSS-synchronized TDMA/FDMA (Frequency-Division Multiple Access)), quantify receiver-side collision risk and detection probability as a function of N, and incorporate spectrum-coordination constraints for multi-node operation.
- Spectrum coordination and licensing. Define the spectrum-use concept for the 28/50 MHz links and initiate IARU (International Amateur Radio Union) amateur-satellite frequency coordination, including identification of suitable amateur allocations and spectral masks. Map the planned modes to applicable national licensing and ITU filing requirements as part of CDR.

7. Conclusions

This paper presents a PlanarSat mission concept for Sporadic-E sensing and documents the early-phase design through Bid, CoDR, and PDR. A consistent power-first method is used across phases to connect per-mode bus power, contingency, and solar-array sizing [25,26], with packaging driven by the no-overlap rule for the planar envelope [16]. Within this framework, the study shows that a two-sided allocation of the same instantaneous MPV widens the operational power envelope under free tumble relative to a single-sided allocation while preserving the simplicity of a single-sensor payload and minimal bus.

The results indicate that feasibility at this scale is governed by surface power and tiling rather than by mass. The link concept and ground-segment assumptions remain unchanged, and the added monitoring and protection functions enable power-aware scheduling without increasing complexity. The PDR baseline therefore focuses on array allocation and operations policy. Future work will close the mechanical envelope for a standard deployer, complete the antenna and inhibit chain, replace bounding link-budget assumptions with measurements, and verify the operational power envelope in hardware before CDR. This analysis supports the conceptual feasibility of a PlanarSat designed specifically for RABSII, contingent on the future validation steps identified (antenna deployment and measured patterns, ground-segment G/T characterization at 28/50 MHz, and on-orbit verification of the batteryless operational power envelope).

Author Contributions: Conceptualization, M.Ş.U.; methodology, M.Ş.U.; software, M.Ş.U.; validation, M.Ş.U.; formal analysis, M.Ş.U.; investigation, M.Ş.U.; resources, M.Ş.U.; data curation, M.Ş.U.; writing—original draft preparation, M.Ş.U.; writing—review and editing, M.Ş.U. and A.R.A.; visualization, M.Ş.U.; supervision, A.R.A.; project administration, M.Ş.U.; funding acquisition, M.Ş.U. and A.R.A. All authors have read and agreed to the published version of the manuscript.

Funding: This research received no external funding.

Institutional Review Board Statement: Not applicable.

Informed Consent Statement: Not applicable.

Data Availability Statement: The original contributions presented in the study are included in the article; further inquiries can be directed to the corresponding author.

Acknowledgments: The authors thank Jurgen Vanhamel for the information he shared about the payload. Additionally, authors thank Onur Çelik, Stefano Speretta and Erdem Turan for their feedback, comments and support.

Conflicts of Interest: The authors declare no conflicts of interest.

Abbreviations

The following abbreviations are used in this manuscript:

ADCS	Attitude Determination and Control System
AIAA	American Institute of Aeronautics and Astronautics
AM0	Air Mass Zero (extraterrestrial solar spectrum)
BiD	Bid/proposal phase (concept feasibility)
CBE	Current Best Estimate (power)
CDR	Critical Design Review
CoDR	Conceptual Design Review
CPFSK	Continuous-Phase Frequency-Shift Keying
CW	Continuous Wave
DC–DC	Direct Current to Direct Current (converter)
EIRP	Effective Isotropic Radiated Power
EPS	Electrical Power System
ESA	European Space Agency
Es	Sporadic-E layer
EsTRACE	Es-layer TRAnsient Cloud Explorer
FDMA	Frequency-Division Multiple Access
FT4	FT4 digital weak-signal mode
FRAM	Ferroelectric Random Access Memory
G/T	Antenna gain-to-noise-temperature ratio
GNSS	Global Navigation Satellite System

GNSS-RO	Global Navigation Satellite System Radio Occultation
HF	High Frequency (3–30 MHz)
IARU	International Amateur Radio Union
JAXA	Japan Aerospace Exploration Agency
LEO	Low Earth Orbit
LNA	Low-Noise Amplifier
MCU	Microcontroller Unit
MEV	Maximum Expected Value
MPPT	Maximum Power Point Tracker
MPV	Maximum Possible Value
NASA	National Aeronautics and Space Administration
NMEA	National Marine Electronics Association
OBC	Onboard Computer
OPE	Operational Power Envelope
PA	Power Amplifier
PCDU	Power Conditioning and Distribution Unit
PDR	Preliminary Design Review
PPS	Pulse Per Second
RAAN	Right Ascension of the Ascending Node
RABSII	Radio Amateur Beacon System for the Investigation of the Ionosphere
RBF	Remove-Before-Flight
RBN	Reverse Beacon Network
RF	Radio Frequency
SNR	Signal-to-Noise Ratio
SSO	Sun-Synchronous Orbit
TDMA	Time-Division Multiple Access
TTC	Telemetry, Tracking, and Command
VHF	Very High Frequency (30–300 MHz)
OpenWebRX	Web-accessible software-defined-radio receiver software
WSPR	Weak Signal Propagation Reporter
WSJT-X	Weak Signal Communication by K1JT

References

1. Vanhamel, J.; Berwaerts, M.; Speretta, S.; Uludag, S. Concept of Sporadic E Monitoring Using Space-Based Low Power Multiple Beacon-Systems. *Atmosphere* **2024**, *15*, 1306. [CrossRef]
2. Haldoupis, C. Midlatitude Sporadic E: A Typical Paradigm of Ionospheric Complexity. *Space Sci. Rev.* **2012**, *168*, 441–461. [CrossRef]
3. Whitehead, J.D. Recent Work on Mid-Latitude and Equatorial Sporadic E. *J. Atmos. Terr. Phys.* **1989**, *51*, 401–424. [CrossRef]
4. International Telecommunication Union. *Handbook on Spectrum Monitoring*; ITU: Geneva, Switzerland, 2019.
5. European Space Agency. *Space Weather Impacts on Radio Communication and Navigation Systems*; European Space Agency: Paris, France, 2021.
6. Pi, X.; Mannucci, A.J.; Lindqwister, U.J.; Ho, C. Monitoring of Global Ionospheric Irregularities Using the Worldwide GPS Network. *Geophys. Res. Lett.* **1997**, *24*, 2283–2286. [CrossRef]
7. Wakabayashi, M.; Ono, T.; Mori, H.; Bernhardt, P.A. Electron density and plasma waves in mid-latitude sporadic-E layer observed during the SEEK-2 campaign. *Ann. Geophys.* **2005**, *23*, 2335–2345. [CrossRef]
8. Haldoupis, C. An Improved Ionosonde-Based Parameter to Assess Sporadic E Layer Intensities: A Simple Idea and an Algorithm. *J. Geophys. Res. Space Phys.* **2019**, *124*, 2127–2134. [CrossRef]
9. Arras, C.; Jacobi, C.; Wickert, J. Semidiurnal tidal signature in sporadic E occurrence rates derived from GPS radio occultation measurements at higher midlatitudes. *Ann. Geophys.* **2009**, *27*, 2555–2563. [CrossRef]
10. Savastano, G.; Nordström, K.; Angling, M.J. Semi-supervised classification of lower-ionospheric perturbations using GNSS radio occultation observations from Spire Global's CubeSat constellation. *J. Space Weather. Space Clim.* **2022**, *12*, 14. [CrossRef]
11. Emmons, D.J.; Wu, D.L.; Swarnalingam, N.; Ali, A.F.; Ellis, J.A.; Fitch, K.E.; Obenberger, K.S. Improved models for estimating sporadic-E intensity from GNSS radio occultation measurements. *Front. Astron. Space Sci.* **2024**, *10*, 1327979. [CrossRef]

12. Klobuchar, J.A. Ionospheric Time-Delay Algorithm for Single-Frequency GPS Users. *IEEE Trans. Aerosp. Electron. Syst.* **1987**, *AES-23*, 325–331. [CrossRef]
13. Rice, D.D.; Sojka, J.J.; Eccles, J.V.; Raitt, J.W.; Brady, J.J.; Hunsucker, R.D. First results of mapping sporadic E with a passive observing network. *Space Weather.* **2011**, *9*, S12001. [CrossRef]
14. American Radio Relay League (ARRL). *The ARRL Handbook for Radio Communications*; ARRL: Newington, CT, USA, 2022.
15. Sweeting, M.N. Modern Small Satellites-Changing the Economics of Space. *Proc. IEEE* **2018**, *106*, 343–361. [CrossRef]
16. Uludağ, M.Ş.; Aslan, A.R. Highly-miniaturized spacecraft "PlanarSat": Evaluating prospects and challenges through a survey of femto & atto satellite missions. *Acta Astronaut.* **2025**, *236*, 343–358. [CrossRef]
17. PUCP Team. *PUCP-Sat-1 & Pocket-PUCP*; Instituto de Radioastronomía, Pontificia Universidad Católica del Perú (PUCP): Lima, Peru. Available online: https://inras.pucp.edu.pe/project/pucp-sat-1-pocket-pucp (accessed on 8 November 2024).
18. Yang, L.; Guo, J.; Fan, C.; Song, X.; Wu, S.; Zhao, Y. The design and experiment of stardust femto-satellite. *Acta Astronaut.* **2020**, *174*, 72–81. [CrossRef]
19. Kacapyr, S. Cracker-sized satellites demonstrate new space tech. *Cornell Chronicle*, 3 June 2019.
20. Manchester, Z.; Peck, M.; Filo, A. KickSat: A Crowd-Funded Mission To Demonstrate The World's Smallest Spacecraft. 2013, SSC13–IX–5. Available online: https://digitalcommons.usu.edu/smallsat/2013/all2013/111/ (accessed on 10 November 2025).
21. Vidal-Valladares, M.G.; Díaz, M.A. A Femto-Satellite Localization Method Based on TDOA and AOA Using Two CubeSats. *Remote Sens.* **2022**, *14*, 1101. [CrossRef]
22. Cumer, M.; Konecny, P.; Novotny, P.; Doskocil, J. Active attitude control for microspacecraft: A survey and new embedded designs. *Adv. Space Res.* **2022**, *69*, 3741–3769. [CrossRef]
23. Barnhart, D.J.; Vladimirova, T.; Baker, A.M.; Sweeting, M.N. A low-cost femtosatellite to enable distributed space missions. *Acta Astronaut.* **2009**, *64*, 1123–1143. [CrossRef]
24. Hein, A.M.; Burkhardt, Z.; Eubanks, T.M. AttoSats: ChipSats, other Gram-Scale Spacecraft, and Beyond. *arXiv* **2019**, arXiv:1910.12559.
25. Uludağ, M.Ş.; Aslan, A.R. Power Contingency/Margin Methodology and Operational Envelope Analysis for PlanarSats. *Aerospace* **2025**, *12*, 858. [CrossRef]
26. Uludağ, M.Ş.; Aslan, A.R. An Analytical Framework for Determining the Minimum Size of Highly Miniaturized Satellites: PlanarSats. *Aerospace* **2025**, *12*, 876. [CrossRef]
27. Taylor, J.; Franke, S.; Somerville, B. *The FT4 Protocol for Digital Contesting*; 22 April 2019. Available online: https://wsjt.sourceforge.io/FT4_Protocol.pdf (accessed on 10 December 2025).
28. Council, N.R. *The Role of Small Satellites in NASA and NOAA Earth Observation Programs*; National Academies Press: Washington, DC, USA, 2000; pp. 42, 54, 59, 62–63. [CrossRef]
29. Wertz, J.R.; Everett, D.F.; Puschell, J.J. (Eds.) *Space Mission Engineering: The New SMAD*; Microcosm Press: Portland, OR, USA, 2011.
30. Franke, S.; Somerville, B.; Taylor, J.H. *The FT4 and FT8 Communication Protocols*; *QEX* 2020, July/August, 7–17 (Issue No. 321); American Radio Relay League (ARRL): Newington, CT, USA. Available online: https://wsjt.sourceforge.io/FT4_FT8_QEX.pdf (accessed on 20 December 2025).
31. International Telecommunication Union. *Recommendation ITU-R SM.1132-2: General Principles and Methods for Sharing Between Radiocommunication Services or Between Radio Stations*; Recommendation SM.1132-2; ITU Radiocommunication Sector (ITU-R): Geneva, Switzerland, 2001.
32. Taylor, J.H. *WSJT-X User Guide*; Version 2.6.0; WSJT Development Group (WSJT-X Project): N.p., 2023. Available online: https://wsjt.sourceforge.io/wsjtx-doc/wsjtx-main-2.6.0.pdf (accessed on 20 December 2025).
33. International Telecommunication Union, Radiocommunication Sector (ITU-R). *Determination of the G/T Ratio for Earth Stations Operating with Communication Satellites*; Technical Report Recommendation S.733-2; ITU-R: Geneva, Switzerland, 2000.
34. International Telecommunication Union, Radiocommunication Sector (ITU-R). *Calculation of Free-Space Attenuation*; Technical Report Recommendation P.525-3; ITU-R: Geneva, Switzerland, 2016.
35. Davies, K. *Ionospheric Radio*; IEE Electromagnetic Waves Series; Peter Peregrinus Ltd.: London, UK, 1990; Volume 31.
36. International Telecommunication Union, Radiocommunication Sector (ITU-R). *Propagation Data and Prediction Methods Required for the Design of Earth-Space Telecommunication Systems*; Technical Report Recommendation ITU-R P.618-14; ITU-R: Geneva, Switzerland, 2023.
37. International Telecommunication Union, Radiocommunication Sector (ITU-R). *Attenuation by Atmospheric Gases and Related Effects*; Technical Report Recommendation ITU-R P.676-12; ITU-R: Geneva, Switzerland, 2019.
38. International Telecommunication Union, Radiocommunication Sector (ITU-R). Radio Noise; Technical Report Recommendation P.372-17; ITU-R: Geneva, Switzerland, 2024.
39. de Oliveira-Costa, A.; Tegmark, M.; Gaensler, B.M.; Jonas, J.; Landecker, T.L.; Reich, P. A model of diffuse Galactic radio emission from 10 MHz to 100 GHz. *Mon. Not. R. Astron. Soc.* **2008**, *388*, 247–260. [CrossRef]

40. The CubeSat Program (Cal Poly SLO). *CubeSat Design Specification (CDS)*; Technical Report, Rev. 13; California Polytechnic State University: San Luis Obispo, CA, USA, 2014. Available online: https://www.cubesat.org/s/cds_rev13_final2.pdf (accessed on 10 September 2025).
41. International Telecommunication Union, Radiocommunication Sector (ITU-R). *Handbook on Small Satellites*; ITU: Geneva, Switzerland, 2023.
42. Broekhuizen, C.H.; Speretta, S.; Uludag, M.S.; van den Bos, M.F.; Haenen, J.; Menicucci, A.; Gill, E.K.A. Miniaturized Radio Tranceiver for PocketQubes, Exceeding Performance of CubeSat Solutions. In Proceedings of the 34th Annual AIAA/USU Conference on Small Satellites (SmallSat 2020), Logan, UT, USA, 1–6 August 2020; Paper SSC20-WKVIII-04.
43. National Renewable Energy Laboratory. *Interactive Best Research-Cell Efficiency Chart*; National Renewable Energy Laboratory: Golden, CO, USA, 2025. Available online: https://www.nrel.gov/pv/interactive-cell-efficiency.html (accessed on 28 November 2025).
44. Speretta, S.; van der Zwaard, R.K.; Uludag, M.S. Autonomous formation flying in the traffic. In Proceedings of the Small Satellites for Earth Observation, Berlin, Germany, 4–8 May.
45. STMicroelectronics. *STM32L496RG—Ultra-Low-Power with FPU Arm Cortex-M4 MCU 80 MHz with 1 Mbyte Flash, USB OTG, LCD, DFSDM*; STMicroelectronics: Geneva, Switzerland, 2024. Available online: https://www.st.com/en/microcontrollers-microprocessors/stm32l496rg.html (accessed on 24 May 2025).
46. Semtech Corporation. *SX1278—137MHz to 525MHz Low Power Long Range Transceiver*; Semtech Corporation: Camarillo, CA, USA, 2024. Available online: https://www.semtech.com/products/wireless-rf/lora-connect/sx1278 (accessed on 24 May 2025).
47. Qorvo, Inc. *SPF5043Z—50 to 4000 MHz General Purpose, Low Noise, Gain Block Datasheet*; Qorvo, Inc.: Greensboro, NC, USA, 2024. Available online: https://www.qorvo.com/products/p/SPF5043Z (accessed on 18 June 2025).
48. Qorvo, Inc. *RFPA0133—380–960 MHz Programmable Gain High-Efficiency Power Amplifier*; Qorvo, Inc.: Greensboro, NC, USA, 2012. Available online: https://www.qorvo.com/products/p/RFPA0133 (accessed on 18 June 2025).
49. Azur Space. *3G30A Triple-Junction Solar Cell Assembly Datasheet*; Azur Space: Germany, 2025. Available online: https://www.azurspace.com/media/uploads/file_links/file/bdb_00010891-01-00_tj3g30-advanced_4x8.pdf (accessed on 18 December 2025).
50. STMicroelectronics. *SPV1040—High-Efficiency Solar Battery Charger with Embedded MPPT*; STMicroelectronics: Geneva, Switzerland, 2021. Available online: https://www.st.com/en/power-management/spv1040.html (accessed on 18 June 2025).
51. STMicroelectronics NV. *High Efficiency Single Inductor Dual Mode Buck-Boost DC-DC Converter with 2.3 A Switches Peak Current—Datasheet*; STMicroelectronics NV: Geneva, Switzerland, 2018; Revision 5. Available online: https://www.st.com/resource/en/datasheet/stbb1-axx.pdf (accessed on 10 September 2025).
52. RAMXEED Limited. *MB85RS4MTY—4 M (512 K × 8) Bit SPI FeRAM Datasheet (AEC-Q100 Compliant)*; RAMXEED Limited: Kanagawa, Japan, 2024. Available online: https://www.ramxeed.com/assets/images/products/datasheet/FeRAM/s2/MB85RS4MTY-GS-DS3v0-E.pdf (accessed on 12 November 2025).
53. Analog Devices, Inc. *LTC4368—100 V UV/OV and Reverse Protection Controller with Bidirectional Circuit Breaker Datasheet*; Analog Devices, Inc.: Wilmington, MA, USA, 2021; Rev. C (04/21). Available online: https://www.analog.com/media/en/technical-documentation/data-sheets/ltc4368.pdf (accessed on 12 November 2025).
54. Texas Instruments Incorporated. *TPS3813xxx Family—Processor Supervisory Circuits with Window-Watchdog Datasheet*; Texas Instruments Incorporated: Dallas, TX, USA, 2024; Rev. J (08/2024), Document number SLVS331J. Available online: https://www.ti.com/lit/ds/symlink/tps3813.pdf (accessed on 12 November 2025).
55. Colagrossi, A.; Lunghi, P.; Pompa, L.; Semprebon, A.; Parissenti, G.; Lavagna, M. FEES: A 1/3U Cubesat Mission for In-Orbit Technology Validation. In Proceedings of the 7th European Conference for Aeronautics and Aerospace Sciences (EUCASS 2017), Milan, Italy, 3–6 July 2017. [CrossRef]
56. Hofman, J.; Sharp, R.; Haze, J. New Techniques for Radiation Testing of CubeSats. In Proceedings of the 6th Interplanetary CubeSat Workshop (iCubeSat 2017), Cambridge, UK, 30 May 2017; Talk B.4.2.
57. Uludag, M.S.; Speretta, S.; Menicucci, A.; Gill, E.K.A. Journey of a PocketQube: Concept to Orbit. In Proceedings of the 34th International Symposium on Space Technology and Science, Kurume, Japan, 3–9 June 2023.
58. Uludag, M.S.; Speretta, S. Delfi-PQ: In-Orbit Performance and Lessons Learned in Developing a 3P PocketQube. In Proceedings of the 76th International Astronautical Congress (IAC 2025), Sydney, Australia, 29 September–3 October 2025; Paper IAC-25-B4-6B-6-x100349.
59. European Space Agency. *Call for a Medium-Size and a Fast Mission in ESA's Science Programme (M7 and F2)—Technical Annex*; Technical Report Technical Annex; European Space Agency (ESA): Paris, France, 2021;
60. NASA Small Spacecraft Systems Virtual Institute (S3VI). 11.0 Ground Data Systems and Mission Operations. 2025. Available online: https://www.nasa.gov/smallsat-institute/sst-soa/ground-data-systems-and-mission-operations/ (accessed on 19 November 2025)
61. Japan Aerospace Exploration Agency (JAXA); *RF Link Design Standard*; Technical Report JERG-2-400A; JAXA Safety and Reliability Promotion Department: Tsukuba, Japan, 2013.

62. Vágner, P.; Urbanec, T.; Kasal, M. Band-monitoring Payload for a CubeSat Satellite. *Radioengineering* **2012**, *21*, 430–435.
63. International Telecommunication Union, Radiocommunication Sector (ITU-R). *Ionospheric Propagation Data and Prediction Methods Required for the Design of Satellite Networks and Systems*; Technical Report Recommendation P.531-16; ITU-R: Geneva, Switzerland, 2025.
64. European Space Agency (ESA). *ECSS-E-ST-70C: Ground Systems and Operations*; Technical Report ECSS-E-ST-70C; European Space Agency (ESA): Noordwijk, The Netherlands, 2008; ECSS Standard for Ground Systems and Operations.
65. ITU. *Reference Link Budgets and Minimum Performance Requirements for Satellite Communications*; ITU-R Recommendation SA.1157-3; International Telecommunication Union: Geneva, Switzerland, 2013;
66. Texas Instruments Incorporated. *INA226—Bi-Directional, Low- or High-Side Measurement, Current/Power Monitor with I^2C Interface*; Texas Instruments: Dallas, TX, USA, 2024. Available online: https://www.ti.com/lit/ds/symlink/ina226.pdf (accessed on 24 May 2025).
67. Texas Instruments Incorporated. *TPS255xx Precision Adjustable Current-Limited Power-Distribution Switches*; Texas Instruments: Dallas, TX, USA, 2024. Available online: https://www.ti.com/lit/ds/symlink/tps2553.pdf (accessed on 24 May 2025).
68. Markley, F.L.; Crassidis, J.L. *Fundamentals of Spacecraft Attitude Determination and Control*; Springer: New York, NY, USA, 2014. [CrossRef]